

# Shallow water equations with depth-dependent anisotropic porosity for subgrid-scale topography

Ilhan Özgen<sup>a,\*</sup>, Dongfang Liang<sup>b,1</sup>, Reinhard Hinkelmann<sup>a</sup>

<sup>a</sup>*Chair of Water Resources and Modeling of Hydrosystems  
Technische Universität Berlin, Germany*

<sup>b</sup>*Department of Engineering  
University of Cambridge, UK*

---

## Abstract

This paper derives a novel formulation of the depth-averaged shallow water equations with anisotropic porosity for computational efficiency reasons. The aim is to run simulations on coarser grids while maintaining an acceptable accuracy through the introduction of porosity terms, which account for subgrid-scale effects. The porosity is divided into volumetric and areal porosities, which are assigned to the cell volume and the cell edges, respectively. The former represents the volume in the cell available to flow and the latter represents the area available to flow over an edge, hence introducing anisotropy. The porosity terms are variable in time in dependence of the water elevation in the cell and the cumulative distribution function of the unresolved bottom elevation. The main novelty of the equations is the formulation of the porosities which enables full inundation of the cell. The applicability of the equations is verified in five computational examples, deal-

---

\*Corresponding author.

*Email address:* [ilhan.oezgen@wahyd.tu-berlin.de](mailto:ilhan.oezgen@wahyd.tu-berlin.de) (Ilhan Özgen)

<sup>1</sup>The research fellowship granted by the Alexander von Humboldt Foundation is gratefully acknowledged.

ing with dam break and rainfall-runoff simulations. Overall, good agreement between the model results and a high-resolution reference simulation has been achieved. The computational time decreased significantly: on average three orders of magnitude.

*Keywords:*

shallow water equations, anisotropic porosity, coarse grid approach, microtopography, integral partial differential equations

---

## 1. Introduction

Shallow water models are applied in a broad range of areas such as river hydraulics [1, 2, 3, 4], dam break simulations [5, 6], urban flooding [7, 8, 9, 10] and recently also for overland flow in natural catchments [11, 12, 13, 14, 15, 16] and urban runoff [17, 18], among many others (cf. e.g. [19]). In overland flow simulations, usually there is a large difference between the scales of the features significantly influencing the flow and the scale of the simulation domain. For example, in a natural catchment with a scale around a square kilometer, local depressions and microtopography with horizontal scales smaller than a square meter influence the flow field significantly [20, 21, 22]. Similar observations are made for urban flood models where the scale of buildings is exceeded by the scale of the city in several orders of magnitude, e.g. a building has a scale of around  $100\text{ m}^2$  while the city may span up to  $100\text{ km}^2$ . Recent developments in survey technology such as light detection and ranging (LIDAR) and laser scanning are able to provide high accuracy high-resolution elevation data sets at relatively low cost [23]. However, the integration of these data into numerical models is often challenging because

of finite computer resources [24, 25]. In order to capture the impact of the smallest relevant scale on the flow, the microtopography has to be explicitly discretized. This leads to meshes with small cell size and therefore high cell number which in return leads to an increased computational effort. Despite developments in CPU power, high-resolution simulations across large catchments are in practice often unfeasible without supercomputers [26].

Instead of explicitly discretizing the small-scale topography, its influence on the flow can be conceptually accounted for on coarser meshes to reduce the computational effort [27]. One such approach introduces a porosity term into the shallow water equations, which refers to the fraction of a computational cell available for flow and is a concept borrowed from groundwater flow modeling. The porosity then conceptually accounts for subgrid-scale topography. In literature, the extended shallow water equations incorporating this porosity are called shallow water equations with porosity or porous shallow water equations. The initial porous shallow water equations have been derived by Defina [11] to account for microtopography in overland flow. Later, the concept has been applied in urban flood modeling as a building treatment method [28, 29, 30, 31, 32, 33, 34]. These porous urban flood models use a single isotropic porosity to account for the buildings in the cell, assuming isotropic behaviour. The reason for this assumption is that the shallow water equations with single porosity are derived from the differential form of the classical shallow water equations using a representative elementary volume (REV) similar to the derivation of the Darcy flow equation in groundwater flow modeling, e.g. [35]. The REV is by definition isotropic and therefore only a single isotropic porosity can be derived for each cell (cf. [29]), which

leads to the loss of directionality and hence may falsify the preferential flow paths. To the authors' knowledge, two approaches have been developed to overcome the loss of directionality and both have been developed for building treatment in urban flood models. The first approach has been developed by Guinot [36] and introduces multiple porosities in each cell, which account for different directions and storages. These porosities can be derived from the differential form of the shallow water equations without violating the continuum model and REV assumption. The second approach has been introduced by Sanders et al. [37]. This approach additionally assigns so-called areal or conveyance porosities to the cell edges, which introduce directionality to the equations. If the differential form of shallow water equations is used, these areal porosities can not be introduced without violating the REV assumption. Therefore, the integral form of the shallow water equations is used, as it does not require the assumption of an REV for the derivation. Yet, using the integral form of the shallow water equations means that only a finite volume method can be utilized for the numerical solution [36, 37]. Because these types of models are not isotropic anymore, they are referred to as anisotropic porosity shallow water models.

While there is ongoing research at the University of Liege to incorporate depth-dependent porosities into an urban flood model [38], the porous shallow water models for building treatment generally do not allow full inundation of the buildings. This is a valid assumption for urban flood modeling, however a porous shallow water model for generalized flow requires partial as well as full inundation of unresolved topography. Therefore, this paper examines the possibility of extending the equations derived in [37] to enable full inundation

of the subgrid-scale unresolved topography to apply it to general surface flow modeling. This leads to a novel formulation of the porosities and the interfacial pressure terms and a mutual dependency between water elevation and porosity.

Finally, it should be noted that the shallow water equations with porosity can not reproduce a high-resolution solution exactly, because they can not resolve local details of the flow. However, the anisotropic porosity model has been found to be able to reproduce overall flow characteristics with satisfactory accuracy.

This paper is organized as follows: first the integral shallow water equations with anisotropic porosity are presented; then the numerical methods are discussed briefly; five computational examples are shown to demonstrate model capabilities; finally conclusions are given. In the following, the unresolved subgrid-scale topography features such as microtopography in overland flow modelling or buildings in urban flood modelling are referred to as unresolved solid structures or unresolved topography.

## **2. Governing equations**

In this section, the integral shallow water equations with anisotropic porosity are derived for an arbitrary control volume. As aforementioned, the numerical solution of the shallow water equations in integral form is only possible with the finite volume method.

### 2.1. Anisotropic porosities

For the derivation of porosity, the phase function  $i$  inside a given control volume is introduced as

$$i(x, y) = \begin{cases} 1, & \text{if } \eta(x, y) > z_b(x, y) \\ 0, & \text{else} \end{cases} \quad (1)$$

where  $\eta$  is the water elevation,  $z_b$  is the bottom elevation and  $x, y$  are the horizontal Cartesian coordinates. Figure 1 illustrates the water elevation  $\eta$  and bottom elevation in a vertical section through a control volume. For illustration purposes,  $i$  is evaluated in two points. If the bottom elevation exceeds the water elevation, i.e. dry case, the phase function is 0. If the water elevation exceeds the bottom elevation, i.e. wet case, the phase function equals 1. Therefore, the phase function indicates whether a certain point  $(x, y)$  in the control volume is wet or dry. Porosity is defined as the ratio of volume or area of fluid to the whole volume or area of the control volume. Then, the volumetric porosity  $\phi$  is defined as

$$\phi = \frac{\int_{\Omega} i(\eta - z_b) d\Omega}{\int_{\Omega} (\eta - z_0) d\Omega} \quad (2)$$

and the areal porosity  $\psi$  of the boundary of the control volume is defined as

$$\psi = \frac{\oint_{\partial\Omega} i(\eta - z_b) dr}{\oint_{\partial\Omega} (\eta - z_0) dr} \quad (3)$$

where  $\Omega$  stands for the area of the control volume,  $\partial\Omega$  stands for the boundary of the control volume,  $z_0$  is the zero datum of the control volume (cf. Figure 1, dashed line) and  $r$  is the path along the boundary  $\partial\Omega$ . The values of the porosities depend on the zero datum  $z_0$ . Here, the lowest bed elevation inside the control volume (denoted as minimum in Figure 1) is chosen as the zero

datum. This means, that in the finite-volume method the zero datum will vary for each cell.

Figure 2 shows an exemplary control volume with the definition of  $\Omega$  and  $\partial\Omega$ . Figure 2 (left) shows a three-dimensional view of a partially inundated control volume, where blue colour indicates the water column and grey colour indicates bottom topography. Figure 2 (right) shows the top view of the control volume (top) and a vertical section through the boundary of the control volume denoted with (A-A') (bottom). Here, darker shades of grey indicate higher bottom elevation. Again, in each point where the water inundates the bottom topography the phase function  $i = 1$  and at the points where the bottom topography elevation exceeds the water elevation  $i = 0$ . Both elevations are calculated with the minimum bottom elevation inside the control volume as the zero datum, which is marked in Figure 2 (left). The volumetric porosity  $\phi$  is calculated with Equation 2, and is the ratio of the volume of the fluid (blue columns) to the volume of the control volume. The volume of the control volume is calculated by multiplying the elevation of the water column, i.e. the distance (A'-B') in Figure 2 (right, bottom) with the total horizontal area of the cell  $\Omega$ , shown in Figure 2 (right, top). For example, in the case illustrated in Figure 2,  $\Omega = (A-A')^2$ . Similarly, the areal porosity  $\psi$  is calculated as the ratio of the vertical area of the fluid at the boundary edge (coloured blue in Figure 2 (right, bottom)) to the vertical area of the boundary, described by the path (A-A'-B'-B) in Figure 2 (right, bottom).

It can be shown that the constant porosities derived in [37] can be obtained by simplifying Equations 2 and 3 (cf. Appendix A). In contrast to

these constant porosities, the porosities derived in this work are variable in time.

## 2.2. Integral-differential form of the shallow water equations with anisotropic porosity

The integral formulation of the shallow water equations can be obtained by applying the balance equation for mass and momentum to a fixed Eulerian control volume under the assumption of hydrostatic pressure distribution [39] (pp. 47 ff.). Prior to the integration, the conserved variables  $h$ ,  $q_x$  and  $q_y$  are multiplied with the phase function  $i$  (Equation 1) to account for the unresolved topography. Then, the temporal change of the vector of conserved variables  $\mathbf{q}$  can be expressed as:

$$\frac{\partial}{\partial t} \int_{\Omega} i \mathbf{q} d\Omega + \oint_{\partial\Omega} i \mathbf{F} \mathbf{n} dr = \int_{\Omega} \mathbf{s} d\Omega + \oint_{\partial\Omega^*} \mathbf{s}^* dr \quad (4)$$

Here,  $t$  is the time and  $\mathbf{s}$  is the source vector.  $\mathbf{q}$  and  $\mathbf{s}$  are usually expressed as:

$$\mathbf{q} = \begin{bmatrix} h \\ q_x \\ q_y \end{bmatrix}, \quad \mathbf{s} = \begin{bmatrix} i_r \\ s_{b,x} + s_{f,x} \\ s_{b,y} + s_{f,y} \end{bmatrix} \quad (5)$$

where  $h = \eta - z_b$  stands for water depth.  $q_x$  and  $q_y$  are the unit discharges in  $x$ - and  $y$ -direction, respectively.  $i_r$  is a mass source term, e.g. rainfall intensity;  $s_{b,x}$ ,  $s_{b,y}$ ,  $s_{f,x}$ ,  $s_{f,y}$  are the bed slope and the friction source terms in  $x$ - and  $y$ -direction, respectively, and are calculated as:

$$s_{b,x} = -gh \frac{\partial z_b}{\partial x}, \quad s_{b,y} = -gh \frac{\partial z_b}{\partial y} \quad (6)$$

$$s_{f,x} = -c_f q_x \frac{\sqrt{q_x^2 + q_y^2}}{h^2}, \quad s_{f,y} = -c_f q_y \frac{\sqrt{q_x^2 + q_y^2}}{h^2} \quad (7)$$

The slope source terms account for variations in bottom and the friction source terms account for the bottom roughness.  $c_f$  stands for the friction coefficient.  $\mathbf{F}$  is the flux vector and can be expressed via  $\mathbf{f}$  and  $\mathbf{g}$  as

$$\mathbf{F}\mathbf{n} = \mathbf{f}n_x + \mathbf{g}n_y \quad (8)$$

where  $\mathbf{n}$  is the unit normal vector to the boundary;  $n_x$  and  $n_y$  are its components and  $\mathbf{f}$  and  $\mathbf{g}$  are the flux vectors in  $x$ - and  $y$ -direction defined as

$$\mathbf{f} = \begin{bmatrix} q_x \\ uq_x + 0.5gh^2 \\ uq_y \end{bmatrix}, \quad \mathbf{g} = \begin{bmatrix} q_y \\ vq_x \\ vq_y + 0.5gh^2 \end{bmatrix}. \quad (9)$$

Here,  $u$  and  $v$  are the depth-averaged velocity in  $x$ - and  $y$ -direction, respectively.  $g$  is the gravitational acceleration.  $\mathbf{s}^*$  is the source vector accounting for fluid pressure along the interface between the fluid and solid  $\partial\Omega^*$ . It results from the macroscopic description, which does not differentiate between fluid and solid (cf. [40], pp. 200-201).

In the limit of no structures to account for, the phase function  $i$  returns 1, the integral along  $\partial\Omega^*$  vanishes and therefore Equation 4 converges to the classical two-dimensional shallow water equations, which can be found in, e.g. [39] (p. 47). In [11], while properties of the differential form of the equations are discussed, it is argued that the equations may fail to give a good approximation for very shallow flow, because some of the assumptions made for the derivation, e.g. a smooth free surface, do not hold. Although the assumptions made in deriving the integral form are not violated during very shallow flow, other statements made in [11] still apply and may lead to an inaccurate approximation. Namely, very shallow flow with partially dry

area is dominated by the effects of bottom irregularities which direct most of water laterally which increases the flow path and the amount of dissipated energy [11]. If these bottom irregularities are only conceptually taken into account by using the porosity and the interfacial pressure terms, the model will not be able to reproduce the correct flow paths and may underestimate the dissipated energy. Unresolved topography which lies inside the computational cell can only be accounted for with the volumetric porosity. This is a limitation of the model, because directionality is introduced in the model in form of the areal porosities, to which the unresolved topography inside the cell can not contribute. Hence, structures which would have influenced the flow direction, e.g. roads and curbs, but lie completely inside the cell, will not effect the flow direction. As a result, their impact on the flow may be underestimated by the model.

### 2.3. Storage and flux terms

The porosity terms in Equation 2 and 3 are used to express discrete forms of the integral terms containing the phase function  $i$ .

The evaluation of the integral of  $i\mathbf{q}$  in Equation 4 is considered. In the following, volume-averaged variables will be used to find a suitable approximation for this integral. The volume-averaged water elevation is calculated as:

$$\bar{\eta} = \frac{\int_{\Omega} i\eta d\Omega}{\int_{\Omega} id\Omega} \quad (10)$$

The volume-averaged velocity is calculated as:

$$\bar{\mathbf{v}} = \frac{\int_{\Omega} ih\mathbf{v}d\Omega}{\int_{\Omega} ihd\Omega} \quad (11)$$

The volume-averaged variables are constant within the control volume  $\Omega$ .

Applying Equation 10 to Equation 2 and using  $\eta - z_b = h$  leads to:

$$\phi = \frac{\int_{\Omega} i(\eta - z_b) d\Omega}{\int_{\Omega} (\eta - z_0) d\Omega} = \frac{\int_{\Omega} ihd\Omega}{\int_{\Omega} (\bar{\eta} - z_0) d\Omega} \quad (12)$$

As established above,  $\bar{\eta}$  is constant inside the control volume. Hence, the expression  $(\bar{\eta} - z_0)$  is also constant inside the control volume and can be taken outside of the integration:

$$\phi = \frac{\int_{\Omega} ihd\Omega}{(\bar{\eta} - z_0) \int_{\Omega} d\Omega} = \frac{\int_{\Omega} ihd\Omega}{(\bar{\eta} - z_0) \Omega} \quad (13)$$

Then, Equation 13 can be rearranged to

$$\int_{\Omega} ihd\Omega = \phi (\bar{\eta} - z_0) \Omega, \quad (14)$$

which corresponds to the evaluation of the integral of the mass storage (first entry of  $\mathbf{q}$ ) in Equation 4. The momentum storage in  $x$ -direction (second entry of  $\mathbf{q}$ ) can be written by using  $q_x = uh$  as:

$$\int_{\Omega} iq_x d\Omega = \int_{\Omega} iuhd\Omega \quad (15)$$

If the velocity  $u$  is approximated by the volume-averaged velocity, the equation becomes:

$$\int_{\Omega} iuhd\Omega \approx \int_{\Omega} i\bar{u}hd\Omega = \bar{u} \int_{\Omega} ihd\Omega \quad (16)$$

Then, Equation 13 can be used to write:

$$\bar{u} \int_{\Omega} ihd\Omega = \phi \bar{u} (\bar{\eta} - z_0) \Omega \quad (17)$$

The same derivation can be applied in  $y$ -direction (third entry of  $\mathbf{q}$  in Equation 4) to get:

$$\int_{\Omega} iq_y d\Omega = \int_{\Omega} ivhd\Omega \approx \int_{\Omega} i\bar{v}hd\Omega = \bar{v} \int_{\Omega} ihd\Omega = \phi \bar{v} (\bar{\eta} - z_0) \Omega \quad (18)$$

The integral of  $\mathbf{q}$  in Equation 4 can be replaced using Equations 13, 17 and 18 to write

$$\frac{\partial}{\partial t} \phi \Omega \bar{\mathbf{q}} + \oint_{\partial\Omega} i \mathbf{F} \mathbf{n} dr = \int_{\Omega} \mathbf{s} d\Omega + \oint_{\partial\Omega^*} \mathbf{s}^* dr, \quad (19)$$

where  $\bar{\mathbf{q}}$  is the vector of volume-averaged variables:

$$\bar{\mathbf{q}} = \begin{bmatrix} (\bar{\eta} - z_0) \\ \bar{u} (\bar{\eta} - z_0) \\ \bar{v} (\bar{\eta} - z_0) \end{bmatrix} \quad (20)$$

The integral of  $i \mathbf{F} \mathbf{n}$  in Equation 4 can be evaluated by defining the area-averaged variables. Here, the area under consideration ( $\partial\Omega$ ) is the boundary of the control volume. The closed curve integral of an arbitrary variable  $q$  can be splitted into integrals along  $n$  segments:

$$\oint_{\partial\Omega} q dr = \int_j^{j+1} q dr + \int_{j+1}^{j+2} q dr + \dots + \int_{j+n}^j q dr \quad (21)$$

This is illustrated in Figure 3, where the black line denotes  $\partial\Omega$  and the blue line denotes a piecewise linear approximation of it. The approximation is intentionally crude for a better illustration. In theory, the integration can be carried out on the splitted parts of  $\partial\Omega$  (Figure 3, black line), however in a finite volume method context the integration is carried out on piecewise linear approximations of the boundary (Figure 3, blue line). The area-averaged variables are calculated as:

$$\hat{h} = \frac{\int_r i h dr}{\int_r i dr} \quad (22)$$

$$\hat{\eta} = \frac{\int_r i \eta dr}{\int_r i dr} \quad (23)$$

$$\hat{\mathbf{v}} = \frac{\int_r i h \mathbf{v} dr}{\int_r i h dr} \quad (24)$$

$r$  is the path between two points on  $\partial\Omega$ , measured counter clockwise around  $\partial\Omega$ , e.g. the path between point  $j$  and  $j + 1$  in Figure 3 (marked with the index  $k + 1$ ). The relationship between  $\partial\Omega$  and  $r$  is that  $\partial\Omega$  is the sum of all paths  $r$ .  $\hat{h}$  is the area-averaged water depth,  $\hat{\eta}$  is the area-averaged water elevation and  $\hat{\mathbf{v}} = (\hat{u}, \hat{v})$  is the area-averaged velocity vector. In a finite volume method, variables would be averaged per cell edge, thus the area would be the edge under consideration. Therefore, the term edge-averaged value is used interchangeably. To differentiate the area-averaged values from the volume-averaged values, the area-averaged values are denoted with a circumflex (hat), e.g.  $\hat{h}$ , and the volume averaged values are denoted with a bar, e.g.  $\bar{h}$ .

The flux term  $\mathbf{F}\mathbf{n}$  in Equation 4 is:

$$\mathbf{F}\mathbf{n} = \begin{bmatrix} q_x n_x + q_y n_y \\ (uq_x + 0.5gh^2) n_x + vq_x n_y \\ uq_y n_x + (vq_y + 0.5gh^2) n_y \end{bmatrix} \quad (25)$$

Equation 3 can be rearranged to:

$$\int_r i(\eta - z_b) dr = \psi \int_r (\eta - z_0) dr \quad (26)$$

Further, applying the relation  $h = \eta - z_b$  and Equation 23 leads to:

$$\int_r ihdr = \psi \int_r (\hat{\eta} - z_0) dr = \psi (\hat{\eta} - z_0) r \quad (27)$$

Equation 24 in combination with Equation 27 can be rearranged to:

$$\int_{\Omega} ih\mathbf{v}dr = \hat{\mathbf{v}} \int_{\Omega} ihdr = \psi \hat{\mathbf{v}} (\hat{\eta} - z_0) r \quad (28)$$

This can be written in  $x$ - and  $y$ -direction as

$$\int_r ihudr = \psi \hat{u} (\hat{\eta} - z_0) r \quad (29)$$

and

$$\int_r ihvdr = \psi\hat{v}(\hat{\eta} - z_0)r, \quad (30)$$

respectively. Using  $q_x = hu$  and  $q_y = hv$ , the integral of the mass flux (first entry of  $\mathbf{F}\mathbf{n}$ ) is approximated as:

$$\int_r (q_x n_x + q_y n_y) dr = \psi\hat{u}(\hat{\eta} - z_0)rn_x + \psi\hat{v}(\hat{\eta} - z_0)rn_y \quad (31)$$

The momentum fluxes (second and third entries of  $\mathbf{F}\mathbf{n}$ ) are approximated by using the area-averaged values  $\hat{h}$ ,  $\hat{u}$  and  $\hat{v}$ . In  $x$ -direction this results in:

$$\int_r (ih\hat{u}\hat{u}n_x + 0.5igh^2n_x + ih\hat{v}\hat{u}n_y) dr \quad (32)$$

The area-averaged values are taken outside of the integral:

$$\hat{u}\hat{u}n_x \int_r ihdr + \int_r 0.5igh\hat{h}n_x dr + \hat{v}\hat{u}n_y \int_r ihdr \quad (33)$$

Equation 27 can be used to rewrite Equation 32:

$$\hat{u}\hat{u}n_x\psi(\hat{\eta} - z_0)r + 0.5g\hat{h}n_x\psi(\hat{\eta} - z_0)r + \hat{v}\hat{u}n_y\psi(\hat{\eta} - z_0)r \quad (34)$$

The approximation of the momentum flux in  $y$ -direction is straight forward. Using Equation 21 to replace the closed curve integral, Equation 19 is rewritten as

$$\frac{\partial}{\partial t}\phi\Omega\bar{\mathbf{q}} + \sum_k \psi_k r_k \hat{\mathbf{F}}_k \mathbf{n}_k = \int_{\Omega} \mathbf{s} d\Omega + \oint_{\partial\Omega^*} \mathbf{s}^* dr, \quad (35)$$

where  $k$  is the index of the path integral. The vector  $\hat{\mathbf{F}}\mathbf{n}$  is written as:

$$\hat{\mathbf{F}}\mathbf{n} = \begin{bmatrix} \hat{u}(\hat{\eta} - z_0)n_x + \hat{v}(\hat{\eta} - z_0)n_y \\ \hat{u}\hat{u}(\hat{\eta} - z_0)n_x + 0.5g\hat{h}(\hat{\eta} - z_0)n_x + \hat{u}\hat{v}(\hat{\eta} - z_0)n_y \\ \hat{v}\hat{u}(\hat{\eta} - z_0)n_x + \hat{v}\hat{v}(\hat{\eta} - z_0)n_y + 0.5g\hat{h}(\hat{\eta} - z_0)n_y \end{bmatrix} \quad (36)$$

#### 2.4. Solid-fluid interfacial pressure source term

$\partial\Omega^*$  is the interface between fluid and solid, denoted with blue lines in Figure 4, where the top view of a square-shaped control volume is given. The dashed black line shows the boundary of the control volume ( $\partial\Omega$ ) and the grey blocks represent single elements of simplified structures, e.g. buildings. Representing the unresolved fluid pressure at the interface  $\partial\Omega^*$ ,  $\mathbf{s}^*$  consists of two components; the stationary component  $\mathbf{s}_{st}^*$  which can be calculated if hydrostatic pressure distribution at the interface is assumed and the non-stationary component  $\mathbf{s}_{ns}^*$  which accounts for drag effects of the unresolved structures [37]:

$$\oint_{\partial\Omega^*} \mathbf{s}^* dr = \oint_{\partial\Omega^*} \mathbf{s}_{st}^* dr + \int_{\Omega} \mathbf{s}_{ns}^* d\Omega \quad (37)$$

While the stationary component  $\mathbf{s}_{st}^*$  acts along the interface  $\partial\Omega^*$ , the non-stationary component acts on the whole control volume  $\Omega$ .

In theory, the calculation of the stationary component  $\mathbf{s}_{st}^*$  is straightforward. Figure 5 shows a vertical section through a control volume and the two possible cases of submergence: partially submerged (left) and fully submerged (right). If these cases are considered separately and hydrostatic pressure is assumed, the pressure of the fluid on the solid  $p^*$  can be written as

$$p^*(x, y) = \begin{cases} 0.5 g (\eta - z_b)^2 & \text{if } \eta(x, y) \leq z_b^* \\ 0.5 g ((\eta - z_b^*) + (\eta - z_b)) (z_b^* - z_b) & \text{else} \end{cases} \quad (38)$$

where  $z_b^*$  is the bottom elevation of the microtopography that the fluid pressure is acting on (cf. Figure 5). If  $\mathbf{m} = (m_x, m_y)$  is the unit normal vector along  $\partial\Omega^*$ , which points inside the solid structure as illustrated in Figure 4, the stationary component of the interfacial pressure source term can be written

as:

$$\mathbf{s}_{st}^* = \begin{bmatrix} 0 \\ p^* m_x \\ p^* m_y \end{bmatrix} \quad (39)$$

The difficulty in the calculation of  $\mathbf{s}_{st}^*$  is that the interface between solid and fluid  $\partial\Omega^*$  is unknown because it is not resolved. Therefore, the stationary term can not be solved exactly and has to be approximated. One approach to estimate  $\mathbf{s}_{st}^*$  can be found in [37].

The non-stationary component of Equation 37 essentially accounts for drag which occurs during the flow through the unresolved structures, e.g. buildings or microtopography, as the fluid moves between the single elements of the structure. Because it occurs at unresolved scales, the drag force can not be calculated. In [37], a generalized drag law is suggested to approximate this term as:

$$\mathbf{s}_{ns}^* = \begin{bmatrix} 0 \\ c_D u |\mathbf{v}| \\ c_D v |\mathbf{v}| \end{bmatrix} \quad (40)$$

Here,  $|\mathbf{v}|$  is the Euclidian norm of the vector of velocities  $\mathbf{v} = (u, v)$  and  $c_D$  is a dimensionless drag coefficient. The determination of  $c_D$  is challenging, often requires a calibration process and has not been fully understood yet. Several approaches have been suggested to overcome this difficulty. In [37], it is acknowledged that the drag effect may be estimated by an increased roughness coefficient as demonstrated in [7]. In [11], momentum correction terms are calculated which depend on the volumetric porosity and a so-called effective water depth, which is the water volume per unit area. Also, different methods with varying complexity for estimating  $c_D$  have been presented in

[28, 29, 30, 37]. In [37], a vegetative resistance model as proposed in [41] is used to estimate  $c_D$ . In this study, the drag force approach is used, because it is commonly used and studied in literature, e.g. [28, 29, 30, 37]. Here, the drag force approach of [41] is slightly modified to allow the full submergence of the control volume. Then,  $c_D$  is calculated as:

$$c_D = 0.5 c_D^0 a \cdot \min(h, z_b^* - z_b) \quad (41)$$

Here,  $a$  is the horizontally projected area of the elements of the solid structure per unit volume in one cell and  $c_D^0$  is a bulk drag coefficient accounting for the whole solid structure (cf. [41]) and  $\min$  is the minimum function. A similar approach is given in [28] to account for inundated subgrid-scale structures. Both  $a$  and  $c_D^0$  are not fully understood yet [37], they depend on the configuration of the solid structures as well as the shape of single elements, flow direction and several other factors which have yet to be identified. Therefore, in this work the model is calibrated with the product  $c_D^0 \cdot a$  as a whole. Hence, both  $a$  and  $c_D^0$  lose their strict physical interpretations and become calibration parameters.

### 3. Numerical method and computational examples

The numerical solution of Equation 35 can only be achieved with the finite volume method, as the equation does not contain spatial differential expressions. Numerical studies of the authors have shown that a second order reconstruction of the bottom elevation is necessary to obtain accurate results, especially in sloped domains (cf. [14]). Further, a second-order accurate scheme allows to compensate to some degree the loss of accuracy

in the approximation due to coarse cells in the anisotropic porosity model. Thus, for the following computational examples, the presented equations are solved with a second-order monotonic upstream-centered scheme for conservation laws (MUSCL) presented in [42] being used for both the anisotropic porosity model and the high-resolution model. It is acknowledged that the high-resolution model is suffering more from the additional calculations per cell associated with the second order reconstruction process in comparison to the anisotropic porosity model. A two-step explicit Runge-Kutta method is used to advance in time [43]. The numerical scheme is implemented in the Hydroinformatics Modeling System (hms), an in-house scientific programming framework [14].

### *3.1. Calculation of porosities*

Similar to [11], it is suggested to calculate the porosities  $\phi$  and  $\psi$  with statistical properties of the unresolved subgrid-scale features of the topography.

In a preprocessing step, the bottom elevation in each computational cell is sampled on a finer scale such that the discrete cumulative distribution function (CDF) can be calculated individually in each cell. The CDF can then be used at the beginning of each time step to evaluate how many of the samples are submerged by the water depth inside the cell. Basically, the CDF is used as a structure to store the different bottom elevations mapped to the number of their occurrences.

For example, let the computational cell have a CDF based on 25 samples of bottom elevation inside the cell. It is assumed that each sample corresponds to an equal area inside the cell. For sake of simplicity, let 10 of the

samples have a bottom elevation of 0, let 10 of the samples have a bottom elevation of 0.2 m and let 5 of the samples have a bottom elevation of 0.4 m. Then, the zero datum in the cell is defined as 0 and the water depth  $h$  in the cell corresponds to the water elevation  $\eta$  as  $h = \eta - 0 = \eta$ . Further, assume the water depth is  $h = 0.1$  m. The volume of the water inside the cell corresponds to  $V_w = 10 \cdot 0.1 \cdot c$ , where  $c$  is the area of one sample. The total volume is  $V_t = 25 \cdot 0.1 \cdot c$ . Then, the volumetric porosity is calculated as  $\phi(h = 0.1) = V_w/V_t = 10/25$ .

If the water depth rises to  $h = 0.3$  m, the volume of water becomes  $V_w = 10 \cdot 0.3 \cdot c + 10 \cdot (0.3 - 0.2) \cdot c$ , and the total volume becomes  $V_t = 25 \cdot 0.3 \cdot c$ . Hence, the volumetric porosity is calculated as  $\phi(h = 0.2) = V_w/V_t = 40/75$ .

The same approach is applied to calculate areal porosities.

### *3.2. Error and speedup calculation*

In the following, computational examples are presented to evaluate the capability of the equations. To the authors' knowledge, no analytical solutions for the shallow water equations with anisotropic porosity have been reported in literature. The shallow water equations with isotropic porosity in [11] are compared with large-scale real case applications. The analytical and semi-analytical solutions presented in [29] are valid for isotropic porosity only. In [37], the anisotropic porosity model results are compared with measurement data.

Therefore, in this work four examples are presented where the high-resolution shallow water model (HR) results are considered to be the reference solution. In a final example, the anisotropic porosity model (AP) results are compared with measurement data. The resolution of the HR model is always

chosen such that further refinement does not change the result. Turbulence and fluid viscosity are neglected in all test cases.

In order to assess the quality of the model results, the  $L_1$ -norm, defined as

$$L_1 = \frac{1}{N} \sum_i^N |x_i - \hat{x}_i| \quad (42)$$

is used, where  $N$  stands for the total number of solutions,  $x_i$  is the reference solution,  $\hat{x}_i$  is the model solution and  $i$  is the sample index.

The computational benefit of the anisotropic porosity model is quantified using the speedup, defined as

$$\zeta = \frac{t_{\text{HR}}}{t_{\text{AP}}} \quad (43)$$

whereby  $t_{\text{HR}}$  and  $t_{\text{AP}}$  are the wall-times of the HR model and the AP model, respectively.

### 3.3. One-dimensional dam break on dry bed with sine-wave shaped microtopography

In this computational example, a one-dimensional dambreak on dry bed is simulated. The domain is 6 m long, 0.5 m wide and the initial water elevation is defined as:

$$\eta(x) = \begin{cases} \eta_0, & x \leq 3 \text{ m} \\ z_b(x), & x > 3 \text{ m} \end{cases} \quad (44)$$

$\eta_0$  stands for the initial water elevation and is varied from 0.025 m to 0.06 m for different simulation runs. The bottom elevation of the domain is described with a sine-wave as:

$$z_b(x) = A \sin\left(\frac{2\pi}{\lambda}x + \frac{\pi}{2}\right) + 0.01 \quad (45)$$

Here,  $\lambda$  is the wavelength and  $A$  is the amplitude of the sine-wave. In this example they are set to  $\lambda = 0.05$  m and  $A = 0.01$  m. Figure 6 (left) shows the initial conditions for  $\eta_0 = 0.03$  m. Only the section from  $2.5 \text{ m} < x < 3.5 \text{ m}$  is plotted because the small wavelength of the sine-wave makes it difficult to illustrate the bottom elevation over the whole domain. At the outlet of the domain at  $x = 6$  m, an open boundary forcing the water elevation gradient to zero is set. All other boundaries are closed boundaries. Bottom roughness is accounted for with a Manning's coefficient of  $n = 0.016 \text{ sm}^{-1/3}$ .

The reference solution is obtained by using a classical shallow water model with an element size of  $\Delta x = 0.01$  m (HR model). As shown in Figure 6 (right), this resolution is sufficient to explicitly discretize the bottom elevation (Equation 45). In contrast, the model with anisotropic porosities (AP model) uses a mesh with element size of  $\Delta x = 0.1$  m. Figure 6 (right) shows exactly one computational cell of the AP model and the bottom topography inside it. The resolution of the AP model's mesh is not sufficient to explicitly discretize the sine-wave, therefore the bottom elevation is described by  $z_b(x) = 0$  m. A classical shallow water model (SWE model) with the same resolution as the AP model is used to illustrate the effect of the AP model. Good agreement between the HR model and the AP model is achieved for  $c_D^0 \cdot a = 10 \text{ m}^2$  as shown in Figure 7 and 8. In [37],  $c_D^0 = 2$  is recommended but values up to  $c_D^0 = 6$  have been reported (M. Bruwer, personal communication, 24 March 2015) which shows that this value has an uncertainty. The results for water elevation, velocity and unit discharge are plotted on the left side in Figure 7 (top, middle and bottom, respectively). The fluctuations in the HR model solution are due to the sine-wave shaped microtopography as

the water accelerates when flowing down the sine-wave and decelerates when climbing up the crests of the sine-wave. The SWE model shows poor agreement in all cases. The AP model captures the advance of the front correctly and the obstructive effects of the microtopography could be reproduced well (Figure 7 (top left)). The velocity is underestimated between  $0 < x < 1$  m and slightly overestimated between  $1 \text{ m} < x < 4$  m (Figure 7 (middle left)). The unit discharge behaves similar as the velocity (Figure 7 (bottom left)). Water elevation, velocity and unit discharge are all captured well. On the right side in Figure 7, the sensitivity of  $c_D^0 \cdot a$  is illustrated. The product  $c_D^0 \cdot a$  is varied from 0 to  $500 \text{ m}^2$ . As  $c_D^0 \cdot a$  increases, the roughness of the model increases. The AP model is sensitive with regard to  $c_D^0 \cdot a$  until a critical value of about  $c_D^0 \cdot a = 500 \text{ m}^2$  is reached. It was observed that for  $c_D^0 \cdot a > 500 \text{ m}^2$  this parameter is not very sensitive. This is because after reaching a certain value, friction is artificially limited in the numerical scheme to avoid velocities to change direction. For details on this friction treatment, the reader is referred to [44].

The initial water elevation  $\eta_0$  is varied to 0.025 m and 0.03 m to study the influence of the water elevation. Figure 8 (left) and Figure 8 (right) show that the solution is enhanced by the AP model for different initial water elevations. In both cases, the overestimation of the velocity and the discharge is higher than for  $\eta_0 = 0.06$  m. It is noted, that the drag coefficient  $c_D^0 \cdot a = 10 \text{ m}^2$  is kept constant for these simulations. Case specific calibration might further enhance the solution. The  $L_1$ -error for the presented cases is summarised in Table 1, 2 and 3 for water elevation, velocity and discharge. For all variables, the  $L_1$ -error of the SWE model is about one order of magnitude higher than

the AP model error. The computation with the AP model was carried out approximately 1000 times faster than with the HR model.

#### 3.4. Two-dimensional dam break across a porosity discontinuity

The following example simulates a two-dimensional dam break across a porosity discontinuity on a  $100 \text{ m} \times 10 \text{ m}$  domain. This example was initially introduced in [29] as a one-dimensional benchmark for the shallow water model with isotropic porosity and a quasi-analytical solution for the one-dimensional case was derived. This solution is not valid for the two-dimensional case, therefore the results of the anisotropic porosity model (AP) is compared with a high-resolution shallow water model (HR). The computational domain is illustrated in Figure 9 (left). The discontinuity of the porosity as well as the discontinuity of the water elevation is located at  $x = 50 \text{ m}$ :

$$\eta_0(x, y) = \begin{cases} 2 \text{ m}, & x \leq 50 \text{ m} \\ 1 \text{ m}, & x > 50 \text{ m} \end{cases} \quad \phi_0(x, y) = \begin{cases} 1, & x \leq 50 \text{ m} \\ 0.8, & x > 50 \text{ m} \end{cases} \quad (46)$$

At the outlet  $x = 100 \text{ m}$ , an open boundary forcing the water elevation gradient to zero is set. All other boundaries are closed wall boundary conditions. The porosity jump is constructed via randomly generated obstacles which are explicitly discretized in the HR model and are taken into account by the porosities in the AP model. All obstacles are square shaped with an edge length of  $0.1 \text{ m}$  and with infinitive vertical height and are spatially distributed according to a random uniform distribution such that each cell of the AP model has a volumetric porosity of  $\phi = 0.8$  for  $x > 50 \text{ m}$  as illustrated in Figure 9 (right) for one exemplary cell. During the whole simulation,

the obstacles are never fully inundated, which means that the volumetric porosity stays constant in each cell. The simulation is run for  $t = 4$  s. The HR model is calculated on a grid with square-shaped elements with an edge length of 0.02 m. The AP model uses a computational grid with square-shaped elements with an edge length of 0.5 m.  $c_D^0 \cdot a = 10 \text{ m}^2$  is chosen for the AP model. Bottom roughness in both models is taken into account by a Manning's coefficient of  $n = 0.016 \text{ sm}^{-1/3}$ .

Results for water elevation and unit discharge at different longitudinal sections at  $t = 4$  s are plotted in Figure 10 (left) and Figure 10 (right), respectively.  $L_1$ -errors for water elevation and unit discharge at the sections are given in Table 4. The AP model results show good agreement with the reference solution calculated by the HR model. After the dam break at  $x = 50$  m, the rarefaction wave traveling in upstream direction as well as the shock wave travelling in flow direction are captured well, although at about  $x = 30$  m the water elevation is underestimated in all sections. The fluctuation of the water elevation, which results from the superposition of waves due to the obstacles, calculated by the HR model can not be reproduced by the AP model. The unit discharge is captured very well by the AP model (Figure 10 (right)). The discretized obstacles in the HR model narrow the cross section available to flow and lead to a high localized flow velocity and therefore a high unit discharge. This can not be reproduced by the AP model. As pointed out in [29], this is not a failure of the AP model, but is a consequence of the macroscopic modeling using the porosity concept. The AP model results were computed roughly 3000 times faster than the HR model results.

### 3.5. Two-dimensional dam break on dry bed with random microtopography

This example considers a two-dimensional dam break on dry bed with random microtopography. The domain spans 6 m in  $x$ -direction and 3 m in  $y$ -direction. The water elevation is defined as:

$$\eta(x) = \begin{cases} 0.03 \text{ m}, & x \leq 3 \text{ m} \\ z_b(x, y), & x > 3 \text{ m} \end{cases} \quad (47)$$

The microtopography is generated as square-shaped deviations with an edge length of 0.05 m, and their amplitudes  $z_{b,mic}$  are distributed between 0 and 0.02 m according to a Gaussian distribution function as illustrated in Figure 11 (right). All boundaries are closed except at the right side of the domain ( $x = 6$  m), where an open boundary condition as in previous the example is applied. A reference solution is computed with a shallow water model on a  $0.01 \text{ m} \times 0.01 \text{ m}$  grid (HR). The anisotropic porosity model uses square grid cells with an edge length of 0.1 m (AP). The bottom friction is expressed via a Manning coefficient  $n = 0.016 \text{ s m}^{-1/3}$ . The drag force of the AP model is estimated with the product  $c_D^0 \cdot a = 10 \text{ m}^2$ . The simulation runs for  $t = 2$  s.

Results for water depth at different sections through different  $y$ -values are plotted in Figure 12. Here, dry cells are not plotted for the HR model. The  $L_1$ -errors for water elevation and velocity at different times are given in Table 5 and 6. The AP model shows very good agreement with the HR model. The shock is captured with satisfactory accuracy at all times, however local details of the water elevation variation such as small scale fluctuations due to the microtopography can not be captured.

Velocity profiles through the same sections as in Figure 12 are plotted in Figure 13. Although the maximum values of the velocity profiles are not

reproduced by the AP model, overall good agreement between the HR model and the AP model is observed.

Figure 14 shows a topview on the water elevation distribution in the domain at the same time steps as in Figure 12 for the HR model (left) and the AP model (right). The HR model resolves the microtopography explicitly and as the water elevation is calculated as  $\eta = h + z_b$ , in the dry part of the domain, the water elevation equals the bottom elevation. It is observed that the overall characteristics of the advancing front and the rarefaction wave moving upstream are captured well by the AP model. However, the spatial distribution of the AP model results have low accuracy, as they suffer from numerical diffusion due to coarse grids as well as the lack of information on small scale bottom elevation variations. The results of the AP model are calculated approximately 1000 times faster than the HR model.

### *3.6. Rainfall-runoff on an inclined plane with random microtopography*

Rainfall-runoff is heavily influenced by the microtopography of the domain [45]. In this example, the surface runoff on a 6 m  $\times$  3 m inclined plane with a slope of 0.02 and a Manning's coefficient of  $n = 0.016 \text{ sm}^{-1/3}$  is simulated. The bottom elevation for the high-resolution model (HR) is calculated as:

$$z_b(x, y) = 1 - 0.02 \cdot x + z_{b,mic}(x, y) \quad (48)$$

Here,  $z_{b,mic}$  is the amplitude of the microtopography, which is generated as square blocks with an edge length of 0.02 m and a vertical amplitude varying between 0 and 0.003 m according to a Gaussian distribution function. The microtopography is applied only inside a rectangular area spanning from

(2.25 m, 0.75 m) to (3.75 m, 2.25 m) whereby the first pair of coordinates denotes the bottom left corner and the latter pair denotes the top right corner of the rectangle as illustrated in Figure 15 (right top). For the anisotropic porosity model (AP), the microtopography is not explicitly discretized and the bottom elevation is calculated as:

$$z_b(x, y) = 1 - 0.02 \cdot x \quad (49)$$

The domain without microtopography is illustrated in Figure 15 (left). Rainfall is imposed for 100 s with the intensity being varied from  $i_r = 1 \cdot 10^{-5}$  m/s to  $i_r = 1 \cdot 10^{-3}$  m/s for different simulation runs. The boundary at the outlet is an open boundary, all other boundaries are closed. The HR model uses a square grid with an element size  $\Delta x = 0.02$  m, the AP model uses a square grid with an element size of  $\Delta x = 0.1$  m. A calibration resulted in  $c_D^0 \cdot a = 0$ , i.e. no drag force influence.

The normalised discharges at the outlet of the domain ( $x = 6$  m) are compared for the different rainfall intensities in Figure 16. The normalized discharge is calculated as the ratio of the model discharge ( $Q_{\text{model}}$ ) to the rainfall discharge, whereby the rainfall discharge for a  $l \times w$  rectangular domain is calculated as [46]:

$$Q_{\text{rain}} = l \cdot w \cdot i_r \quad (50)$$

The comparison shows that the influence of the microtopography is overestimated by the AP model. In the early time of the simulation, both hydrographs agree well but when the wave which is influenced by the microtopography reaches the outlet the hydrographs start to deviate.

For  $i_r = 1 \cdot 10^{-5}$  m/s the AP model does not reach its concentration time in 100s. The agreement at the late stages of the simulation (after  $t = 80$ s) is less good. This suggests that in the AP model, the influence of the microtopography is overestimated in these test cases and thus the water is artificially held back and does not reach the outlet. This argument is supported by the fact that the agreement gets better for increasing rainfall intensity, cf. e.g. the hydrograph of  $i_r = 1 \cdot 10^{-3}$  m/s. As the intensity increases, the influence of the microtopography on the flow decreases. For  $i_r = 1 \cdot 10^{-4}$  m/s the hydrograph of the AP model rises a little bit too slow and for  $i_r = 1 \cdot 10^{-3}$  m/s both hydrographs agree well. The water depths behave similarly. The results of the AP model are on average computed 550 times faster than the reference solution.

The  $L_1$ -errors for different intensities are given in Table 7. Here, the  $L_1$ -error is divided by the corresponding intensity for better comparison of the cases.

For  $i_r = 1 \cdot 10^{-4}$  m/s, model results at different points are compared (cf. Figure 17, right bottom). Figure 17 also shows a comparison of normalized discharges at these evaluation points. Good agreement between the discharges is observed at the points 1, 2 and 5. However, especially at points 1 and 2 is a temporal delay in the hydrograph of the AP model which again comes from the overestimation of the influence of microtopography. Point 3, which is located inside the area with microtopography, shows the worst agreement which might result from the aforementioned overestimation as well as the macroscopic approach of the AP model which is not expected to reproduce local flow processes. At point 4 the discharge is overshoot by the AP

model.

Model results for the same points are compared in Figure 18 for  $i_r = 1 \cdot 10^{-5}$  m/s. Here, it is seen that the agreement at the points where the flow is influenced by the microtopography, namely points 2, 3 and 4, gets worse for lower intensities. Especially at point 3, which is located inside the area with microtopography, the AP model returns a discharge which is 3 times higher than the HR model discharge and is temporally delayed.

The  $L_1$ -errors at the different points are given in Table 8 and 9 for  $i = 10^{-4}$  m/s and  $i = 10^{-3}$  m/s, respectively. Again, the  $L_1$ -errors are divided by the corresponding intensity.

Figure 19 shows temporal snapshots of the discharge distribution in the domain at  $t = 15$  s,  $t = 20$  s and  $t = 50$  s for both the HR model (left) and the AP model (right). The resolution of the AP model is much coarser than the HR model and therefore local details can not be resolved as good as in the HR model but general properties of the flow field are reproduced. At  $t = 20$  s the overestimation of microtopography can be seen very clearly, as the flow calculated by the HR model (Figure 19, left middle) has already reached the right border of the microtopography area while the flow calculated by the AP model (Figure 19, right middle) has only reached the middle of the microtopography area. The discharge of the AP model is higher than of the HR model, however the porosity slows down the front of the AP model flow. This can also be observed in Figure 17 (left middle), where the discharge at point 3 is delayed and overestimated by the AP model. At  $t = 50$  s the flow fields reasonably resemble (Figure 19, bottom).

### 3.7. Dam-break flow through an idealised city

In this computational example, results of a dam-break experiment conducted at the Université catholique de Louvain, Belgium, [47] are numerically reproduced.

#### 3.7.1. Domain description, initial and boundary conditions

The domain is a 35.8 m long and 3.6 m wide channel with horizontal bed. The idealised city consists of  $5 \times 5$  buildings, each of them being a square block with an edge length of 0.30 m. The distance between the blocks is 0.10 m. The dam-break is constructed by opening a 1 m wide gate, which initially separates part of the channel with water ponding at 0.40 m from the rest of the channel (reservoir), where a very thin layer of 0.011 m water due to imperfect tightness of the gate is reported. For further details on the experimental setup and employed measurement techniques, the reader is referred to [47]. The domain is illustrated in Figure 20, where the reservoir is coloured in grey.

For the numerical model, only the reservoir and the first 16 m of the channel is discretised for computational efficiency. In preliminary studies it had been observed that for the duration of the simulations,  $t = 15.5$  s, the shock wave does not travel further than this length. The downstream boundary is an open boundary and all other boundaries are closed boundaries.

The HR model uses a triangular mesh with three different cell sizes: the inside of the reservoir is discretised with cells with a characteristic length of  $l_{c,1} = 0.3$  m. The area inside the channel which is sufficiently far away from the building blocks is discretised with a characteristic length of  $l_{c,2} = 0.1$  m. The space between the buildings is discretised with a characteristic length of

$l_{c,3} = 0.01$  m. The buildings are represented as holes in the mesh, which is a method commonly used in urban flood modeling [48]. With the value chosen for  $l_{c,3}$ , the space between two buildings is discretised with about 10 cells and the total cell number is 95975. The AP model uses square-shaped cells with an edge length of 0.25 m in the whole domain, which results in 1272 cells in total.

Experimental data is available at 64 measurement gauges distributed inside the channel [47]. The positions of these gauges are given in Figure 21. Errors are calculated for all gauges. In the discussion, results are plotted only for 4 gauges, namely gauges 1, 18, 44 and 55, to avoid too many figures. These gauges are pointed out in Figure 21.

The roughness of the channel has been estimated in [47] with a Manning’s coefficient of  $n = 0.01 \text{ sm}^{1/3}$ . This value is used for both the HR and the AP model.

### 3.7.2. Model calibration and run time

The AP model is calibrated with the value  $a \cdot c_D^0$ . The best results in this specific case were obtained by completely neglecting the drag force, i.e.  $a \cdot c_D^0 = 0$ . No calibration is carried out for the HR model. The HR model simulation takes about 3000 s wall-clock time to finish. The AP model requires about 4 s wall-clock time. Consequently, the speedup is calculated as 750 (cf. 10).

### 3.7.3. Discussion

The HR model makes overall a good prediction of the water depth at the evaluated gauges. In Figure 22, the water depth calculated by the HR

model at the aforementioned gauges is plotted together with the measured water depth. Overall, the numerical results approximate the experimental results very well. The arrival time of the wave is predicted correctly at all gauges. Larger deviations between the results occur at the later stages of the simulation. At gauge 18, which is located between the buildings, the wave reflections from the walls of the buildings superpose and create several peaks between  $t = 3.5\text{ s}$  and  $t = 6.5\text{ s}$  in the HR model results which were not observed during the experiment. Further, at gauge 1, which is at the upper right corner of the building block, the water depth is underestimated by the HR model. This might be because of the hydraulic jump observed at the impact section which leads to increased local water levels which are not reproduced by the HR model. These points might raise the question, whether a turbulence model should be used, however Soares-Frazão and Zech [47] report that adding turbulence to the numerical model leads to a worse agreement between numerical and experimental results.

The anisotropic porosity model (AP) shows good agreement with the HR model results, although the results of the AP model are smoother and more diffused than the HR model results. In Figure 22, AP model results for water depth are plotted for the four gauges as well. Gauge 1 and gauge 18 show very good agreement, while the arrival time of the wave at gauge 44 is delayed. Gauge 55, located in the front of the building block, shows the worst agreement of the four. Here, the AP model overshoots the HR model. The peak at around  $t = 4\text{ s}$  is not reproduced. Overall, the general properties of the AP model results, i.e. the lack of local and spatial fluctuations, agree with the observations in [49]. In general, the AP model error manifests itself

in excessive damping of the results.

$L_1$ -errors of both models in regard to the experimental data are calculated as the average  $L_1$ -error of all 64 gauges. The HR model has a  $L_1$ -error of 0.02 m, the AP model has a  $L_1$ -error of 0.07 m.

#### 4. Conclusions

An integral formulation of the two-dimensional shallow water equations with anisotropic porosity for flow over partially and fully inundated topography was derived. A novel formulation for the porosities was proposed and an approximation for the storage and flux terms was presented. The porosities are dependant on the water elevation in the cell. This relationship can be approximated by calculating a cumulative distribution function for the unresolved bottom elevation and evaluating it at the water elevation. Due to the macroscopic point of view, additional terms appear in the governing equations. Suitable approximations for these terms have been referred to. The non-stationary term was approximated with a drag force approach. The integral formulation of the equations can only be solved by the finite volume method. A second order MUSCL scheme was used to solve the equations with a two-step explicit Runge-Kutta method for time stepping.

Five computational examples, ranging from simple academic benchmarks to nearly 'real case' laboratory experiments were shown to demonstrate the capabilities and limitations of the new approach. Due to the lack of analytical solutions a high-resolution shallow water model was used to calculate reference solutions. In the last test case, experimental data was used for model evaluation. The shallow water model with porosity showed overall

good agreement with the reference solutions. The aforementioned drag term was used to calibrate the model and a sensitivity study regarding this term was carried out. Except in the last test case, good results are obtained with  $c_D^0 \cdot a = 10$ . However, further studies to investigate the drag force coefficient values and the possibility to represent the drag effect with increased friction are required.

As bottom slope increases, the accuracy of the anisotropic shallow water model decreases. Experimental studies show that a large bed slope reduces the effect of microtopography [50] and the presented model seems to underestimate the reduction.

A challenge in practical applications is the isolation of the part of topography modeled as porosity from the global topography. Usually, the global topography is defined as the roughness of the surface of the earth and represented by the cell value. The unresolved topography is thought about as subgrid-scale deviations from this value which creates heterogeneity inside the cell. The issue of identifying these deviations has been researched in the context of isolating microtopography and different methods have been proposed in the literature, e.g. [51]. However, finding suitable methods to correctly isolate the part of topography to be modeled as porosity remains an open issue, which seems to be the main limitation of applying the proposed model to 'real world cases'.

Local details of the flow could not be exactly reproduced by the anisotropic porosity model, because the concept of porosity as a statistical property of the topography is not expected to reproduce processes at this scale [29].

The novel anisotropic porosity was found to be a good balance between

computational time and accuracy. Table 10 gives an overview of the speedups in the simulations in dependency of cell size  $\Delta x$  and cell number  $n$ . The ratio of cell numbers ( $n_{\text{HR}}/n_{\text{AP}}$ ) is identified as the main factor of the speedup. In the presented computational examples, the anisotropic porosity model provided a computational benefit around three orders of magnitude, depending on the ratio of the cell numbers, i.e. the difference in cell size.

## 5. Acknowledgement

The authors thank Prof. Andrea Defina, Università degli Studi di Padova, Italy, for the insightful personal communication, and the Local Organizing Committee of the Advances in Numerical Modelling of Hydrodynamics Workshop, Sheffield, UK, guest editor Dr. Daniel Caviedes-Voullième and the anonymous reviewers for their valuable comments.

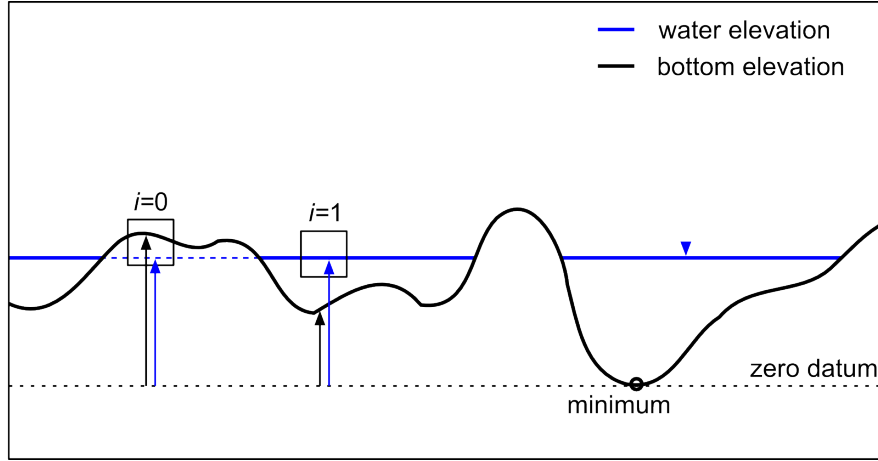


Figure 1: Definition of phase function  $i$ , water elevation  $\eta$  (blue), bottom elevation  $z_b$  (black) and zero datum  $z_0$  (dashed) in a vertical section through a control volume

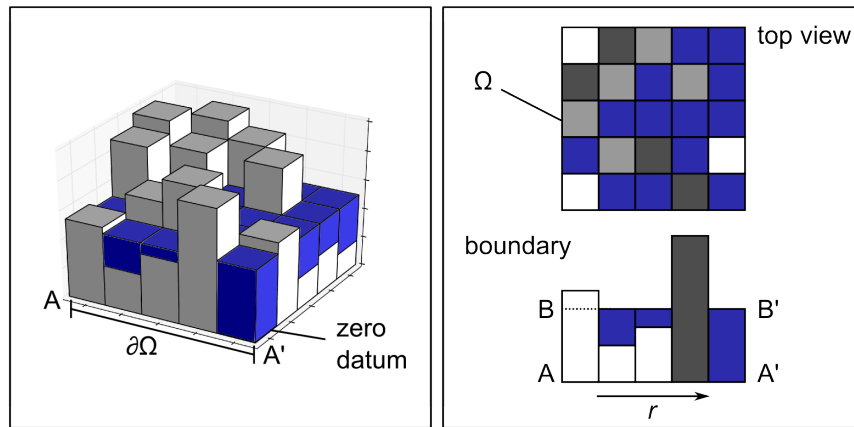


Figure 2: Definition of control volume area  $\Omega$ , control volume boundary  $\partial\Omega$  and path  $r$  in three dimensional view (left) top view and vertical section through the cell edge marked with A-A' (right)

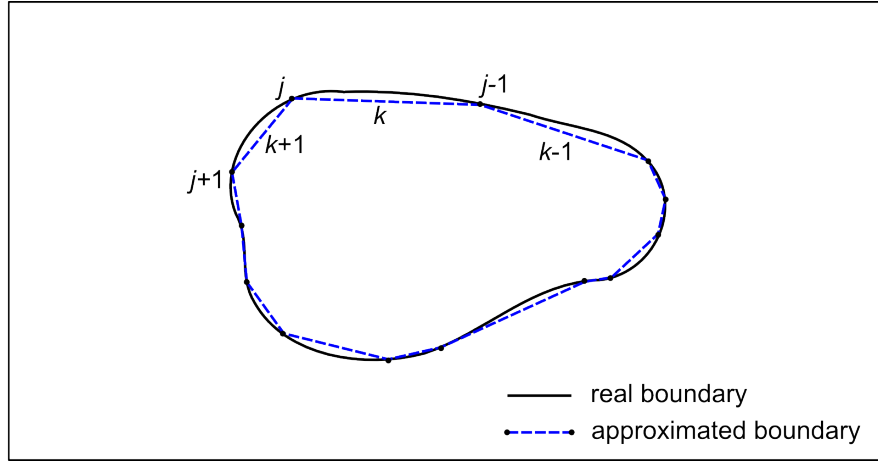


Figure 3: Definition of path index  $k$  and vertex index  $j$ : top view of an arbitrary control volume; black color indicates the exact boundary, blue color indicates the approximated boundary

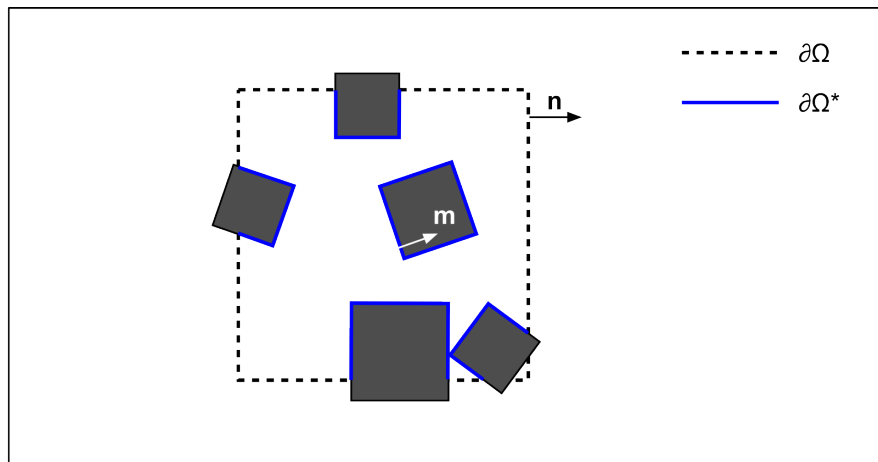


Figure 4: Definition of the interface  $\partial\Omega^*$  (blue); grey blocks represent elements of microtopography

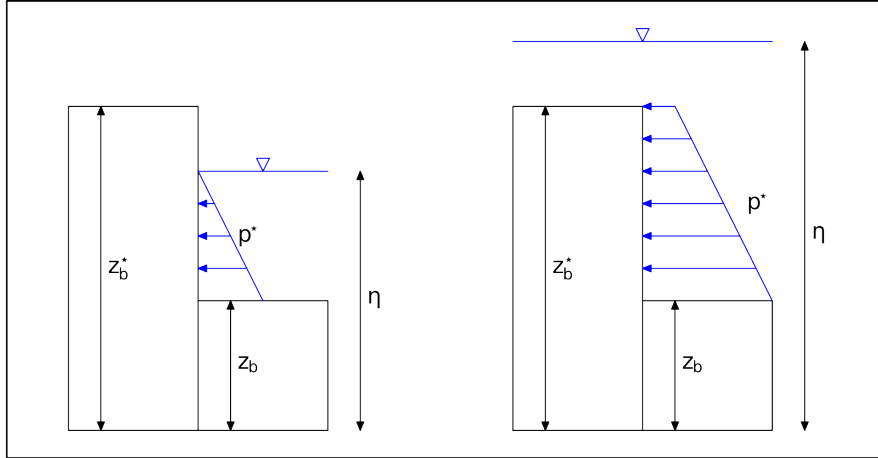


Figure 5: Definition of  $p^*$  and  $z_b^*$ ; partially submerged control volume (left), fully submerged control volume (right): blue color indicates the water column

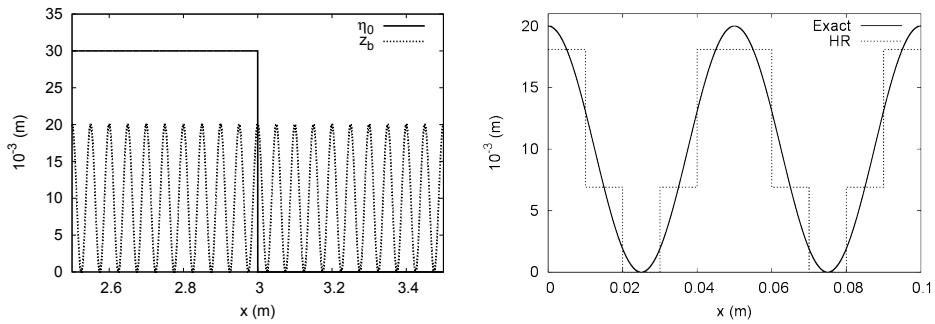


Figure 6: Dam break on dry bed with sine-wave shaped microtopography: Initial conditions for  $\eta_0 = 0.03$  m (left); bottom elevation distribution inside one AP model cell and the HR model discretization (dashed lines) (right)

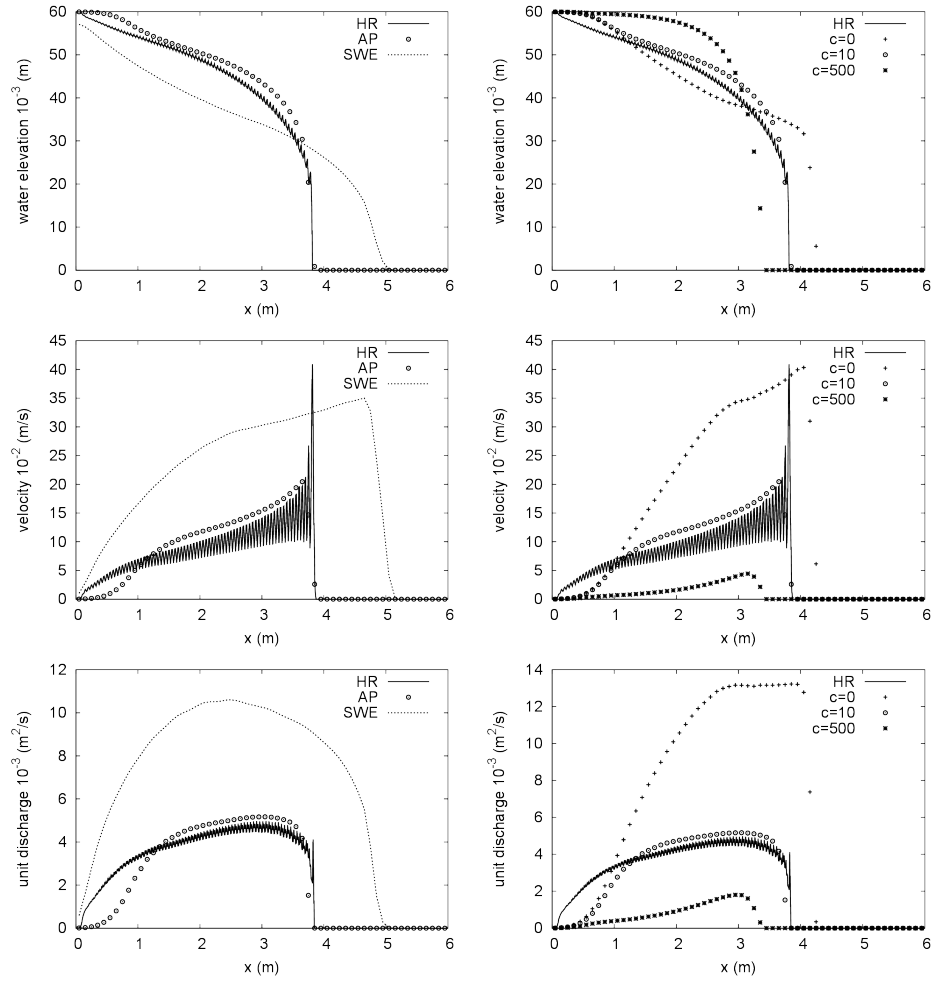


Figure 7: Dam break on dry bed with sine-wave shaped microtopography: Comparison of model results at  $t = 4$  s with  $\eta_0 = 0.06$  m (the anisotropic porosity model (AP), the high-resolution reference solution (HR) and a coarse grid classical shallow water model (SWE)) (left), sensitivity study of  $c_D^0 \cdot a$  (denoted as  $c$ ) (right)

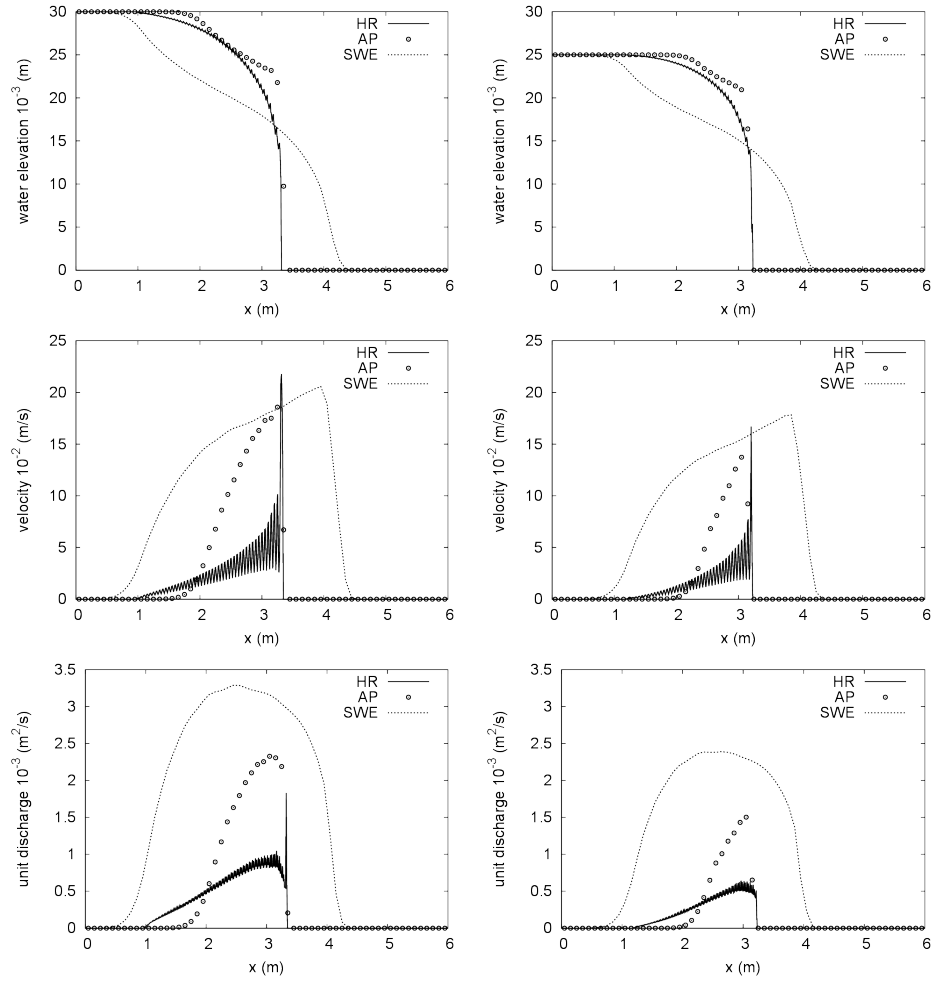


Figure 8: Dam break on dry bed with sine-wave shaped microtopography: Comparison of model results at  $t = 4$  s with  $\eta_0 = 0.03$  m (left) and  $\eta_0 = 0.025$  m (right) (the anisotropic porosity model (AP), the high-resolution reference solution (HR) and a coarse grid classical shallow water model (SWE))

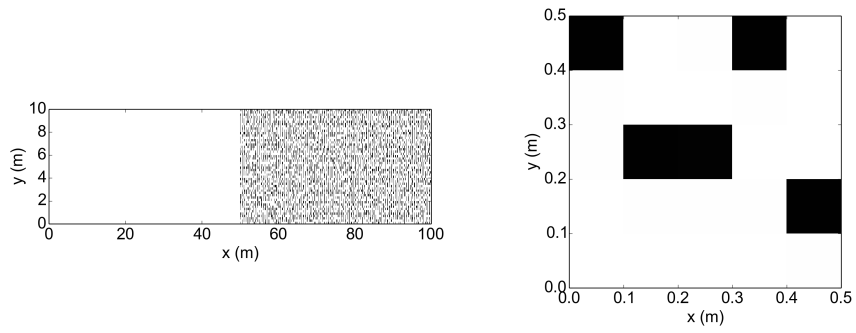


Figure 9: Dam break across a porosity discontinuity: Top view on the computational domain (left); top view on an exemplary computational cell of the AP model (right), black color indicates the location of obstacles

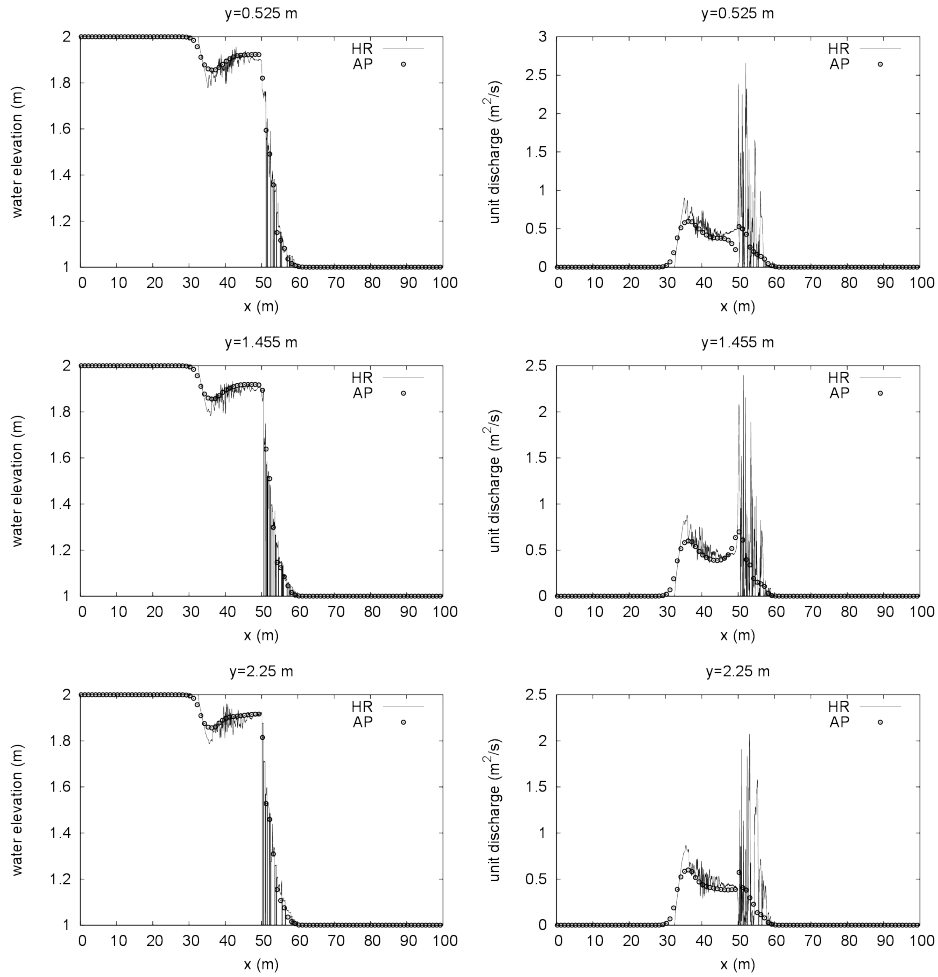


Figure 10: Dam break across a porosity discontinuity: Water elevation (left) and unit discharge (right) at  $t = 4$  s for different longitudinal sections for the anisotropic porosity model (AP) and the high-resolution reference solution (HR)

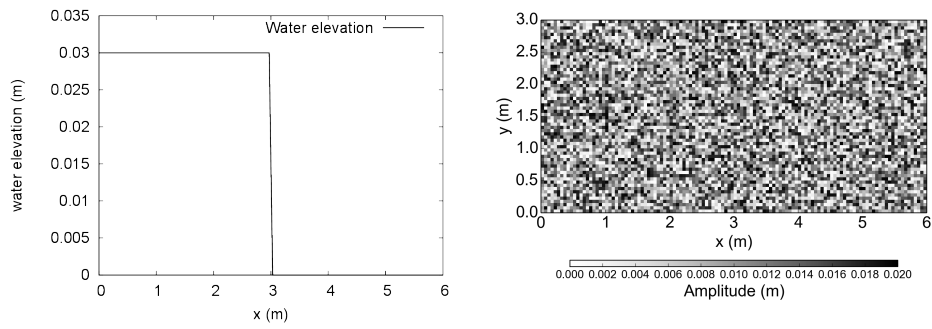


Figure 11: Dam break on bed with random microtopography: Initial conditions (left); microtopography in the domain (right)

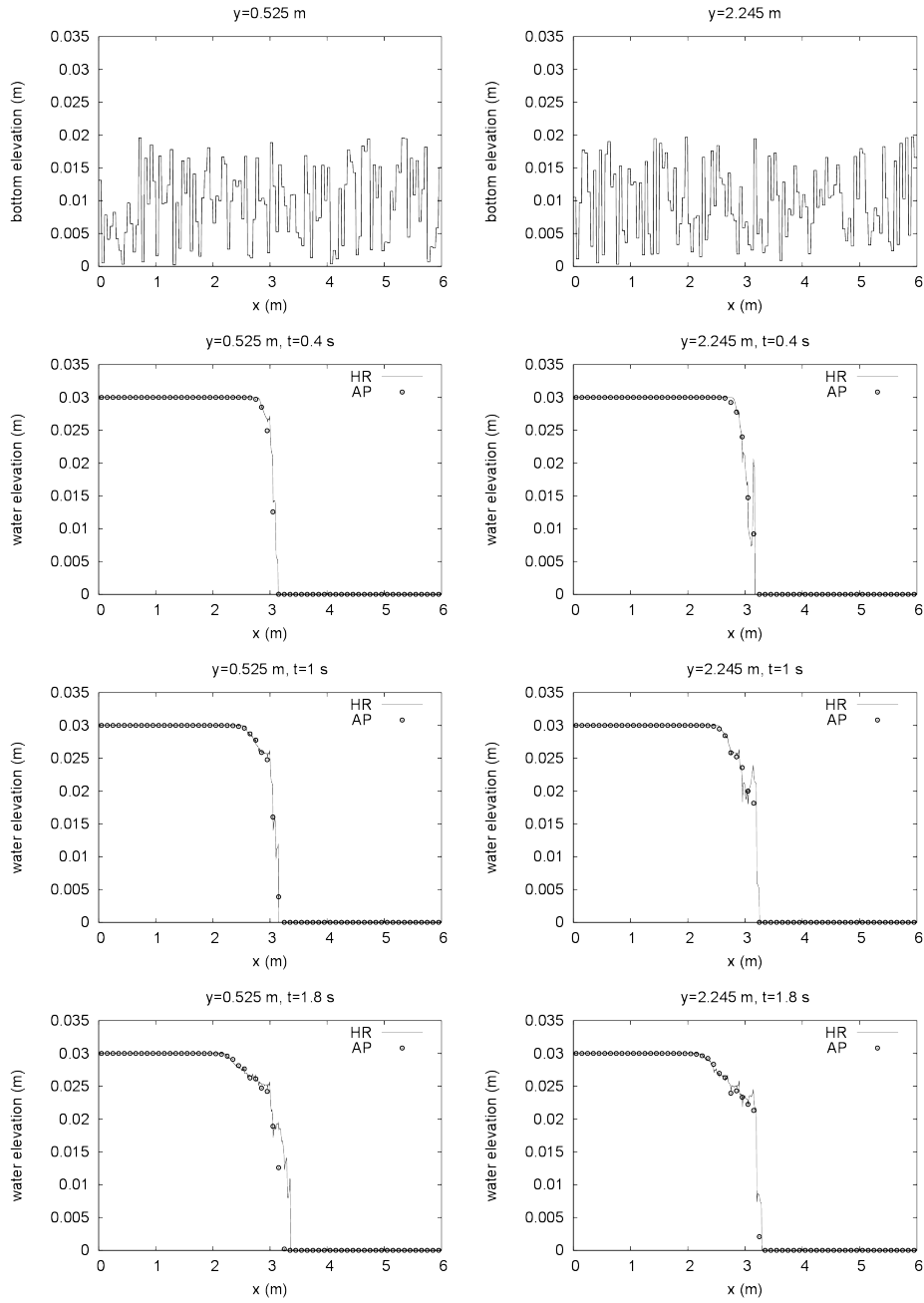


Figure 12: Dam break on bed with random microtopography: Water elevations at  $y = 0.525$  m (left) and  $y = 2.245$  m (right) at different times for the anisotropic porosity model (AP) and the high-resolution reference solution (HR); the high-resolution bottom topography is plotted at the very top of each column for illustration purposes

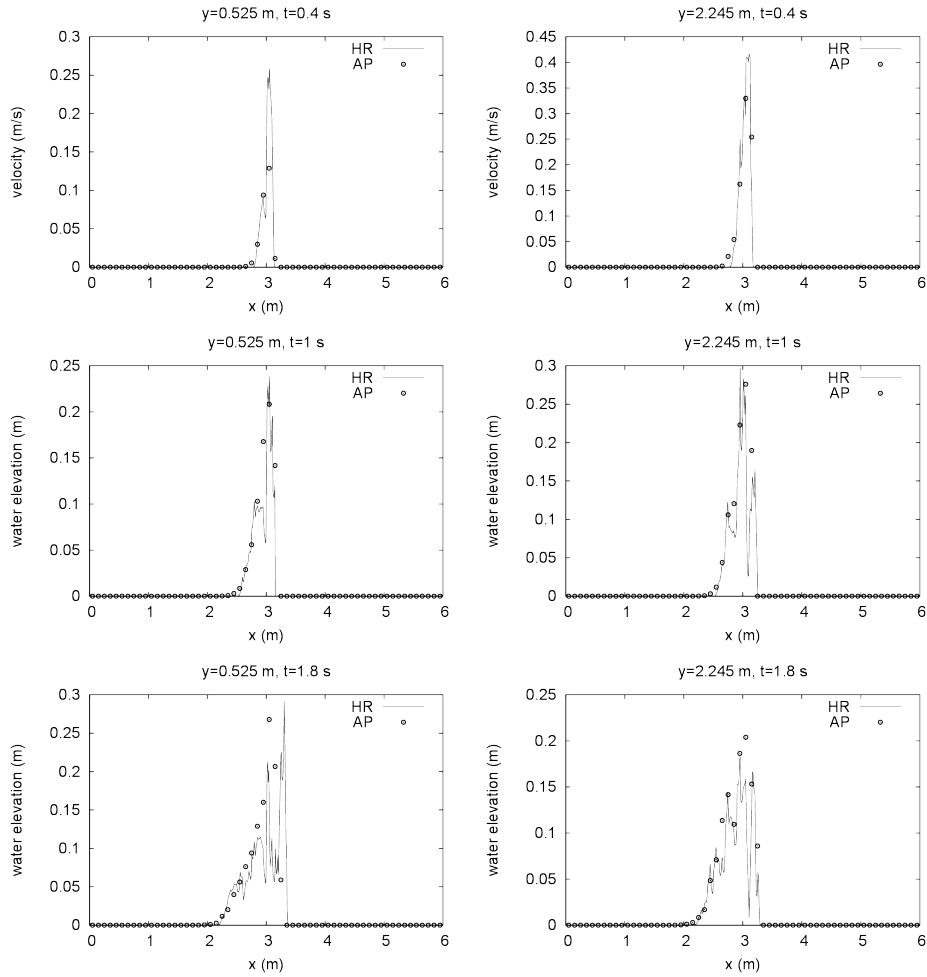


Figure 13: Dam break on bed with random microtopography: Flow velocities at  $y = 0.525$  m (left) and  $y = 2.245$  m (right) at different times for the anisotropic porosity model (AP) and the high-resolution reference solution (HR)

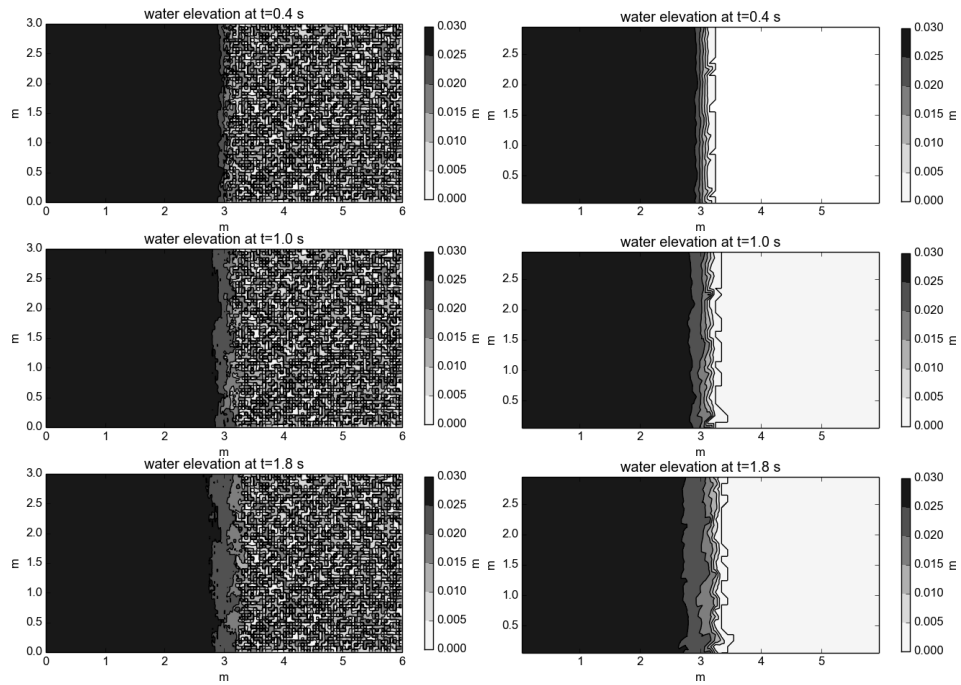


Figure 14: Dam break on bed with random microtopography: Water elevations at different time steps for the high-resolution reference solution (HR) (left) and the anisotropic porosity model (AP) (right)

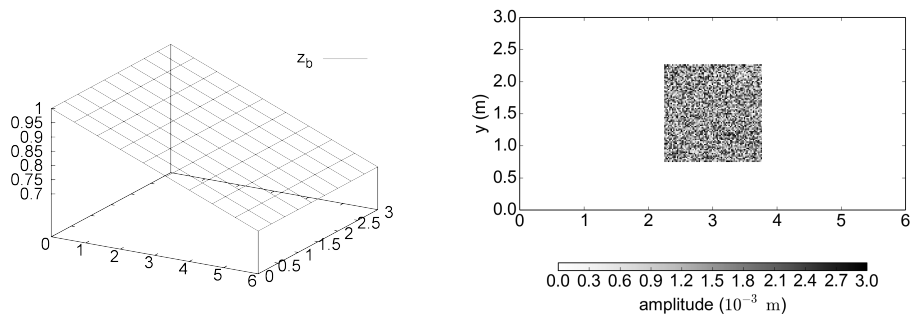


Figure 15: Rainfall-runoff on an inclined plane with random microtopography: Side view of the computational domain without microtopography (left); top view of the position and spatial distribution of microtopography (right top); top view of the positions of evaluation points (right bottom)

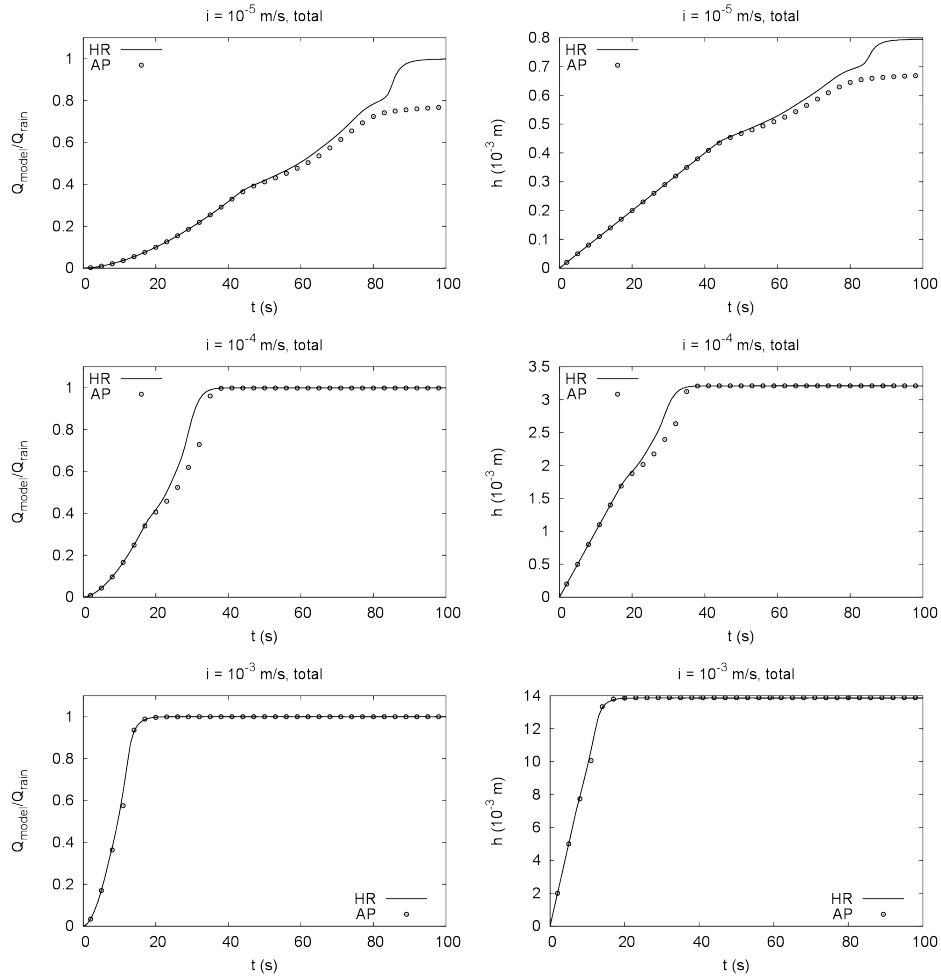


Figure 16: Rainfall-runoff on an inclined plane with random microtopography: Comparison of normalized discharges (left) and water depths (right) at the outlet computed by the HR model and the AP model for different rainfall intensities

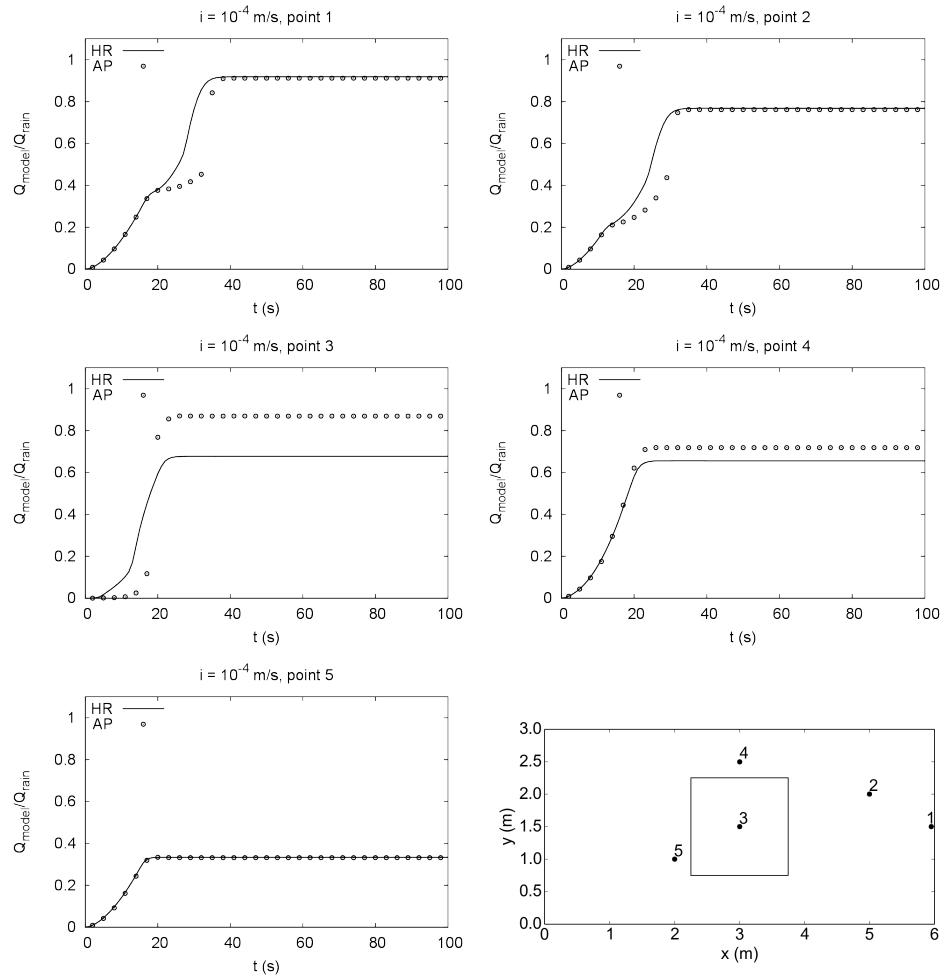


Figure 17: Rainfall-runoff on an inclined plane with random microtopography: Comparison of normalized discharges computed by the HR model and the AP model for  $i_r = 1 \cdot 10^{-4}$  m/s at different evaluation points (plotted in the right bottom)

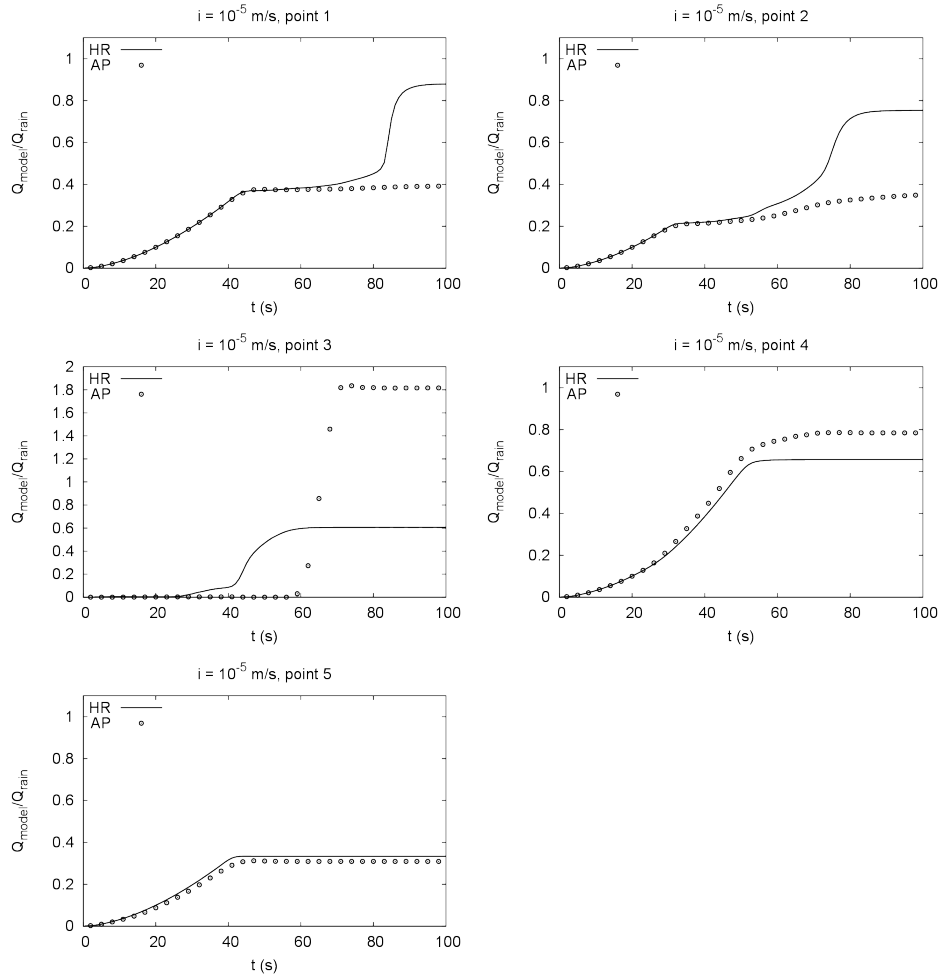


Figure 18: Rainfall-runoff on an inclined plane with random microtopography: Comparison of normalized discharges computed by the HR model and the AP model for  $i_r = 1 \cdot 10^{-5}$  m/s at different evaluation points (plotted in the right bottom of Figure 17)

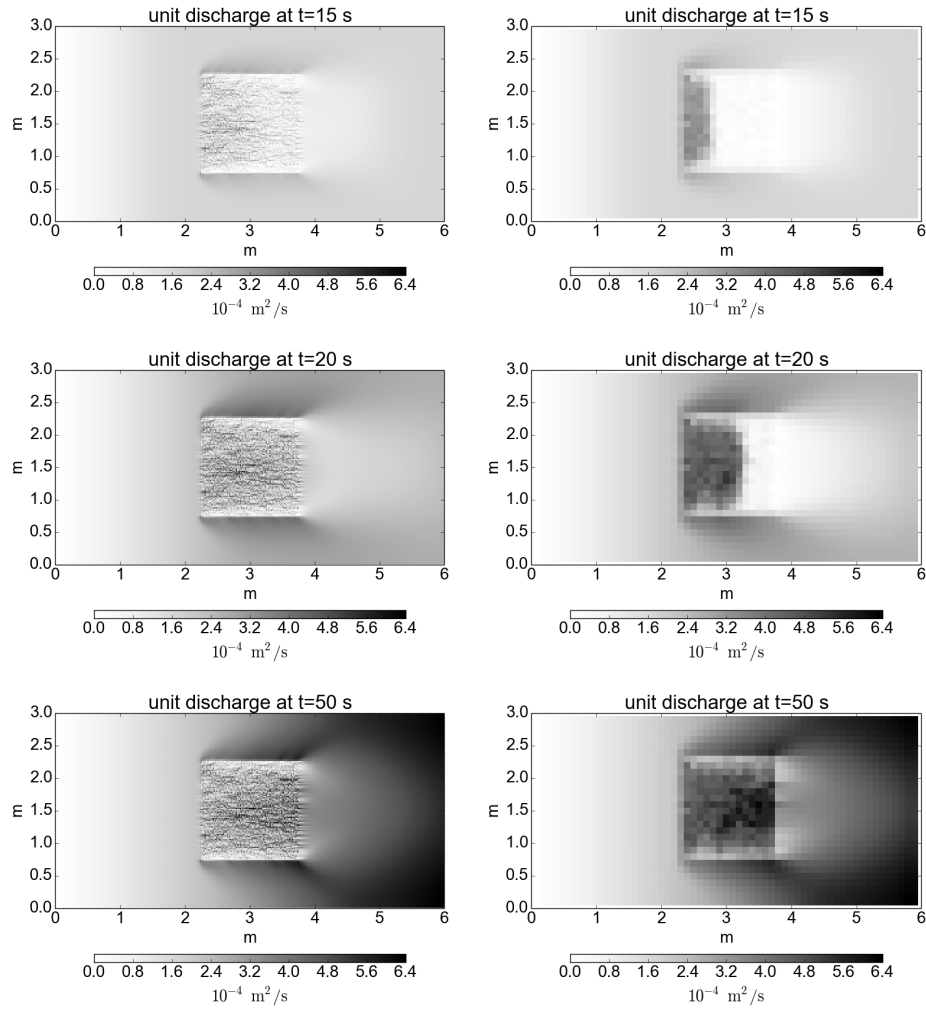


Figure 19: Rainfall-runoff on an inclined plane with random microtopography: Comparison of snap shots of unit discharges computed by the HR model (left) and the AP model (right) at different time steps

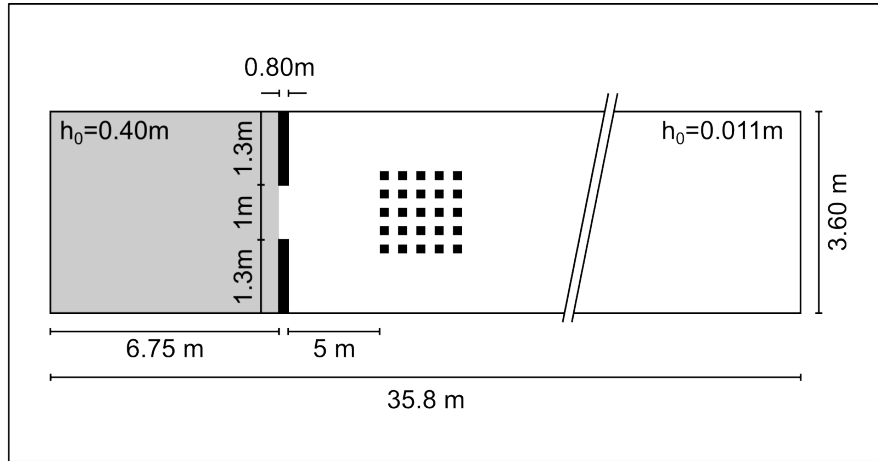


Figure 20: Dam break flow through an idealised city: Computational domain and initial conditions

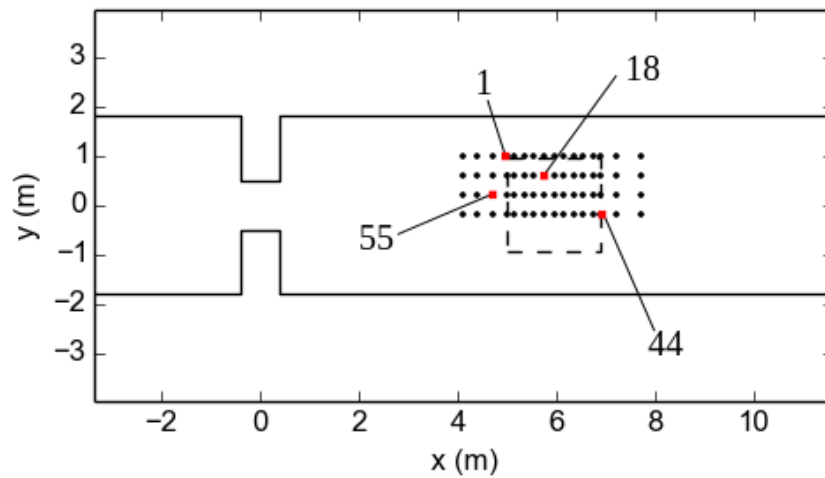


Figure 21: Dam break flow through an idealised city: Location of the gauges, area of building array is marked with dashed line

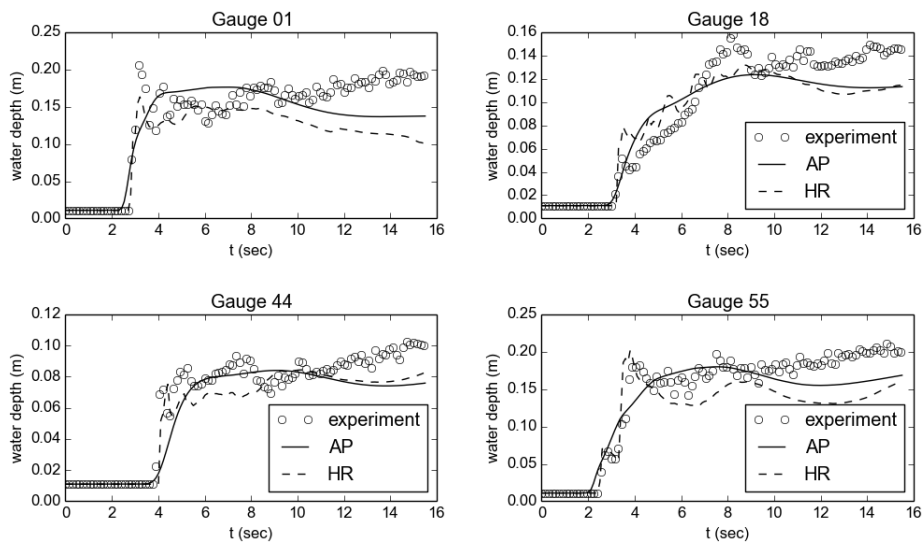


Figure 22: Dam break flow through an idealised city: Discharges calculated by the anisotropic porosity model (AP), high-resolution model (HR) and the measurement data at gauges 1, 18, 44 and 55

$\eta$ (m)	$L_{1,AP}(\eta)$ (m)	$L_{1,SWE}(\eta)$ (m)
0.025	$3.8 \cdot 10^{-4}$	$28 \cdot 10^{-4}$
0.03	$6.4 \cdot 10^{-4}$	$34 \cdot 10^{-4}$
0.06	$15 \cdot 10^{-4}$	$76 \cdot 10^{-4}$

Table 1: Dam break on dry bed with sine-wave shaped microtopography:  $L_1$ -error for water elevation as calculated by the anisotropic porosity model (AP) and the coarse shallow water model (SWE)

$\eta$ (m)	$L_{1,AP}(v)$ (m/s)	$L_{1,SWE}(v)$ (m/s)
0.025	$0.8 \cdot 10^{-2}$	$5.7 \cdot 10^{-2}$
0.03	$1.6 \cdot 10^{-2}$	$7 \cdot 10^{-2}$
0.06	$1.2 \cdot 10^{-2}$	$13.8 \cdot 10^{-2}$

Table 2: Dam break on dry bed with sine-wave shaped microtopography:  $L_1$ -error for velocity as calculated by the anisotropic porosity model (AP) and the coarse shallow water model (SWE)

$\eta$ (m)	$L_{1,AP}(q)$ (m <sup>2</sup> /s)	$L_{1,SWE}(q)$ (m <sup>2</sup> /s)
0.025	$1.0 \cdot 10^{-4}$	$8.6 \cdot 10^{-4}$
0.03	$2.6 \cdot 10^{-4}$	$12 \cdot 10^{-4}$
0.06	$4.9 \cdot 10^{-4}$	$44 \cdot 10^{-4}$

Table 3: Dam break on dry bed with sine-wave shaped microtopography:  $L_1$ -error for unit discharge as calculated by the anisotropic porosity model (AP) and the coarse shallow water model (SWE)

$y$ (m)	$L_1(\eta)$ (m)	$L_1(q)$ (m <sup>2</sup> /s)
0.525	$8.1 \cdot 10^{-3}$	$5.3 \cdot 10^{-2}$
1.455	$7 \cdot 10^{-3}$	$3.9 \cdot 10^{-2}$
2.25	$7.4 \cdot 10^{-3}$	$5.3 \cdot 10^{-2}$

Table 4: Dam break on dry bed across a porosity discontinuity:  $L_1$ -error for water elevation and unit discharge

$t$ (s)	$L_1(\eta)$ (m)	$L_1(v)$ (m/s)
0.4	$1.8 \cdot 10^{-4}$	$2 \cdot 10^{-3}$
1	$2.5 \cdot 10^{-4}$	$3.6 \cdot 10^{-3}$
1.8	$6 \cdot 10^{-4}$	$9.1 \cdot 10^{-3}$

Table 5: Dam break with random microtopography:  $L_1$ -error for water elevation and velocity for  $y = 0.525$  m

$t$ (s)	$L_1(\eta)$ (m)	$L_1(v)$ (m/s)
0.4	$2.7 \cdot 10^{-4}$	$4 \cdot 10^{-3}$
1	$2.5 \cdot 10^{-4}$	$5 \cdot 10^{-3}$
1.8	$2 \cdot 10^{-4}$	$6 \cdot 10^{-3}$

Table 6: Dam break with random microtopography:  $L_1$ -error for water elevation and velocity for  $y = 0.525$  m

$i$ (m/s)	$L_1(q)$ ((m <sup>2</sup> /s)/(m/s))	$L_1(h)$ (m/(m/s))
$10^{-3}$	$1.4 \cdot 10^{-2}$	$3.8 \cdot 10^{-2}$
$10^{-4}$	$10 \cdot 10^{-2}$	$40 \cdot 10^{-2}$
$10^{-5}$	$28 \cdot 10^{-2}$	$280 \cdot 10^{-2}$

Table 7: Rainfall-runoff on an inclined plane with random microtopography: scaled  $L_1$ -error for unit discharge and water elevation at the outlet, errors are scaled by division by the corresponding rainfall intensity

point	$L_1(q)$ ((m <sup>2</sup> /s)/(m/s))
1	$2 \cdot 10^{-1}$
2	$1.6 \cdot 10^{-1}$
3	$10 \cdot 10^{-1}$
4	$3.1 \cdot 10^{-1}$
5	$0.13 \cdot 10^{-1}$

Table 8: Rainfall-runoff on an inclined plane with random microtopography: scaled  $L_1$ -error for unit discharge at the gauges for  $i = 10^{-4}$  m/s, errors are scaled by division by the rainfall intensity

point	$L_1(q) ((\text{m}^2/\text{s})/(\text{m}/\text{s}))$
1	$5.1 \cdot 10^{-1}$
2	$7.2 \cdot 10^{-1}$
3	$30 \cdot 10^{-1}$
4	$4 \cdot 10^{-1}$
5	$1.2 \cdot 10^{-1}$

Table 9: Rainfall-runoff on an inclined plane with random microtopography: scaled  $L_1$ -error for unit discharge at the gauges for  $i = 10^{-5}$  m/s, errors are scaled by division by the rainfall intensity

Case	$\Delta x_{\text{HR}}$	$n_{\text{HR}}$	$\Delta x_{\text{AP}}$	$n_{\text{HR}}$	$n_{\text{HR}}/n_{\text{AP}}$	speedup
3.3	0.01 m	30000	0.1 m	300	100	1000
3.4	0.02 m	2500000	0.5 m	4000	625	3000
3.5	0.01 m	180000	0.1 m	1800	100	1000
3.6	0.02 m	45000	0.1 m	1800	25	550
3.7	0.01 – 0.3 m	95975	0.25 m	1272	75.4	750

Table 10: Summary of speedups obtained in all simulations,  $n$ : Number of cells,  $\Delta x$ : edge length, HR: high-resolution model, AP: anisotropic porosity model

## Appendix A. Derivation of porosities by Sanders *et al.* [37]

It can be shown that the definitions of porosity in [37] can be considered as a special case of Equations 2 and 3, where submergence of microtopography is not allowed. If microtopography is not allowed to be submerged, the wet fraction of the control volume will remain constant. Further, if the wet fraction of the control volume is considered to have the same constant bed elevation  $z_b = z_0$ , Equation 2 can be simplified to

$$\phi = \frac{\int_{\Omega} i (\eta - z_0) d\Omega}{\int_{\Omega} (\eta - z_0) d\Omega} = \frac{(\eta - z_0) \int_{\Omega} i d\Omega}{(\eta - z_0) \int_{\Omega} d\Omega} = \frac{1}{\Omega} \int_{\Omega} i d\Omega. \quad (\text{A.1})$$

If the same assumptions are made for the boundary of the control volume, Equation 3 simplifies to

$$\psi = \frac{\oint_{\partial\Omega} i (\eta - z_0) dr}{\oint_{\partial\Omega} (\eta - z_0) dr} = \frac{1}{\partial\Omega} \oint_{\partial\Omega} i dr. \quad (\text{A.2})$$

Equations A.1 and A.2 are the porosities introduced in [37] for building treatment. The assumptions made are valid for describing the effects of buildings, which are unlikely to become submerged by the flood wave. If the porosities are used to describe the effects of microtopography, Equations 2 and 3 have to be used. A significant difference between Equations 2 and 3 (with inundation) and Equations A.1 and A.2 (without inundation) is that the porosities that allow inundation are dependent on the water elevation  $\eta$ , which is variable in time. If the water elevation increases, the porosities increase. Therefore, the porosities are functions of time if the terrain variation within a control volume is considered and inundation is allowed, while without inundation the wet fraction of the control volume remains constant and thus, the porosities are constant in time.

## References

- [1] I. Özgen, S. Seemann, A. L. Candeias, H. Koch, F. Simons, R. Hinkelmann, Simulation of hydraulic interaction between Icó-Mandantes bay and São Francisco river, Brazil, in: G. Gunkel, J. A. A. Silva, M. d. C. Sobral (Eds.), Sustainable Management of Water and Land in Semiarid Areas, Editora Universitária UFPE, Recife, Brazil, 2013, Ch. 1.2, pp. 28–38.
- [2] G. Kesserwani, Q. Liang, RKDG2 shallow-water solver on non-uniform grids with local time steps: Application to 1D and 2D hydrodynamics, *Applied Mathematical Modelling* 39 (3-4) (2015) 1317–1340. doi:10.1016/j.apm.2014.08.009.
- [3] C. Lange, M. Schneider, M. Mutz, M. Haustein, M. Halle, M. Seidel, H. Sieker, C. Wolter, R. Hinkelmann, Model-based design for restoration of a small urban river, *Journal of Hydro-environmental Research (JHER)* 9 (2) (2015) 226–236.
- [4] G. Petaccia, L. Natale, F. Savi, M. Velickovic, Y. Zech, S. Soares-Frazão, Flood wave propagation in steep mountain rivers, *Journal of Hydroinformatics* 15 (1) (2013) 120. doi:10.2166/hydro.2012.122.
- [5] C. Zoppou, S. Roberts, Numerical solution of the two-dimensional unsteady dam break, *Applied Mathematical Modelling* 24 (7) (2000) 457–475. doi:10.1016/S0307-904X(99)00056-6.
- [6] Y. Liu, J. Zhou, L. Song, Q. Zou, L. Liao, Y. Wang, Numerical modelling of free-surface shallow flows over irregular topography with com-

- plex geometry, *Applied Mathematical Modelling* 37 (23) (2013) 9482–9498. doi:10.1016/j.apm.2013.05.001.
- [7] D. Liang, R. A. Falconer, B. Lin, Coupling surface and subsurface flows in a depth averaged flood wave model, *Journal of Hydrology* 337 (1-2) (2007) 147–158. doi:10.1016/j.jhydrol.2007.01.045.
- [8] D. Liang, X. Wang, R. a. Falconer, B. N. Bockelmann-Evans, Solving the depth-integrated solute transport equation with a TVD-MacCormack scheme, *Environmental Modelling and Software* 25 (12) (2010) 1619–1629. doi:10.1016/j.envsoft.2010.06.008.
- [9] Q. Liang, Flood simulation using a well-balanced shallow flow model, *Journal of Hydraulic Engineering* 136 (9) (2010) 669–675. doi:10.1061/(ASCE)HY.1943-7900.0000219.
- [10] G. Petaccia, S. Soares-Frazão, F. Savi, L. Natale, Y. Zech, Simplified versus Detailed Two-Dimensional Approaches to Transient Flow Modeling in Urban Areas, *Journal of Hydraulic Engineering* 136 (2010) 262–266. doi:10.1061/(ASCE)HY.1943-7900.0000154.
- [11] A. Defina, Two-dimensional shallow flow equations for partially dry areas, *Water Resources Research* 36 (11) (2000) 3251–3264. doi:10.1029/2000WR900167.
- [12] C. Mügler, O. Planchon, J. Patin, S. Weill, N. Silvera, P. Richard, E. Mouche, Comparison of roughness models to simulate overland flow and tracer transport experiments under simulated rain-

- fall at plot scale, *Journal of Hydrology* 402 (1-2) (2011) 25–40. doi:10.1016/j.jhydrol.2011.02.032.
- [13] P. Costabile, C. Costanzo, F. Macchione, Comparative analysis of overland flow models using finite volume schemes, *Journal of Hydroinformatics* 14 (1) (2012) 122–135. doi:10.2166/hydro.2011.077.
- [14] F. Simons, T. Busse, J. Hou, I. Özgen, R. Hinkelmann, A model for overland flow and associated processes within the Hydroinformatics Modelling System, *Journal of Hydroinformatics* 16 (2) (2014) 375–391. doi:10.2166/hydro.2013.173.
- [15] D. P. Viero, P. Peruzzo, L. Carniello, A. Defina, Integrated mathematical modeling of hydrological and hydrodynamic response to rainfall events in rural lowland catchments, *Water Resources Research* doi:10.1002/2013WR014293.
- [16] I. Özgen, K. Teuber, F. Simons, D. Liang, R. Hinkelmann, Upscaling the shallow water model with a novel roughness formulation, *Environmental Earth Sciences Thematic issue* (2015) 1–16. doi:10.1007/s12665-015-4726-7.
- [17] L. Cea, M. Garrido, J. Puertas, Experimental validation of two-dimensional depth-averaged models for forecasting rainfallrunoff from precipitation data in urban areas, *Journal of Hydrology* 382 (1-4) (2010) 88–102. doi:10.1016/j.jhydrol.2009.12.020.
- [18] D. Liang, I. Özgen, R. Hinkelmann, Y. Xiao, J. M. Chen, Shallow water simulation of overland flows in idealised catchments, *Environmental*

- Earth Sciences Thematic issue (2015) 1–12. doi:10.1007/s12665-015-4744-5.
- [19] J. Hou, Q. Liang, H. Zhang, R. Hinkelmann, An efficient unstructured MUSCL scheme for solving the 2D shallow water equations, *Environmental Modelling and Software* 66 (2015) 131–152. doi:10.1016/j.envsoft.2014.12.007.
- [20] T. Dunne, W. Zhang, B. F. Aubry, Effects of rainfall, vegetation, and microtopography on infiltration and runoff, *Water Resources Research* 27 (9) (1991) 2271–2285.
- [21] G. Blöschl, M. Sivapalan, Scale issues in hydrological modelling: a review, *Hydrological Processes* 9 (1995) 251–290.
- [22] S. E. Thompson, G. G. Katul, A. Porporato, Role of microtopography in rainfall-runoff partitioning: An analysis using idealized geometry, *Water Resources Research* 46 (7). doi:10.1029/2009WR008835.
- [23] P. Gourbesville, Data and hydroinformatics: new possibilities and challenges, *Journal of Hydroinformatics* 11 (34) (2009) 330–343. doi:10.2166/hydro.2009.143.
- [24] F. Dottori, G. Di Baldassarre, E. Todini, Detailed data is welcome, but with a pinch of salt: Accuracy, precision, and uncertainty in flood inundation modeling, *Water Resources Research* 49 (9) (2013) 6079–6085. doi:10.1002/wrcr.20406.

- [25] H. K. McMillan, J. Brasington, Reduced complexity strategies for modelling urban floodplain inundation, *Geomorphology* 90 (3-4) (2007) 226–243. doi:10.1016/j.geomorph.2006.10.031.
- [26] L. S. Smith, Q. Liang, Towards a generalised GPU/CPU shallow-flow modelling tool, *Computers & Fluids* 88 (2013) 334–343. doi:10.1016/j.compfluid.2013.09.018.
- [27] L. D’Alpaos, A. Defina, Mathematical modeling of tidal hydrodynamics in shallow lagoons: A review of open issues and applications to the Venice lagoon, *Computers & Geosciences* 33 (4) (2007) 476–496. doi:10.1016/j.cageo.2006.07.009.
- [28] J.-M. Hervouet, R. Samie, B. Moreau, Modelling urban areas in dam-break flood-wave numerical simulations, in: *International Seminar and Workshop on Rescue Actions based on Dambreak Flood Analysis*, Vol. 1, Seinäjoki, Finland, 2000.
- [29] V. Guinot, S. Soares-Frazão, Flux and source term discretization in two-dimensional shallow water models with porosity on unstructured grids, *International Journal for Numerical Methods in Fluids* 50 (3) (2006) 309–345. doi:10.1002/fld.1059.
- [30] S. Soares-Frazão, J. Lhomme, V. Guinot, Y. Zech, Two-dimensional shallow-water model with porosity for urban flood modelling, *Journal of Hydraulic Research* 46 (1) (2008) 45–64. doi:10.1080/00221686.2008.9521842.

- [31] L. Cea, M.-E. Vázquez-Cendón, Unstructured finite volume discretization of two-dimensional depth-averaged shallow water equations with porosity, *International Journal for Numerical Methods in Fluids* 63 (2009) 903–930. doi:10.1002/fld.2107.
- [32] A. S. Chen, B. Evans, S. Djordjević, D. a. Savić, A coarse-grid approach to representing building blockage effects in 2D urban flood modelling, *Journal of Hydrology* 426-427 (2012) 1–16. doi:10.1016/j.jhydrol.2012.01.007.
- [33] A. S. Chen, B. Evans, S. Djordjević, D. a. Savić, Multi-layered coarse grid modelling in 2D urban flood simulations, *Journal of Hydrology* 470-471 (2012) 1–11. doi:10.1016/j.jhydrol.2012.06.022.
- [34] J. E. Schubert, B. F. Sanders, Building treatments for urban flood inundation models and implications for predictive skill and modeling efficiency, *Advances in Water Resources* 41 (2012) 49–64. doi:10.1016/j.advwatres.2012.02.012.
- [35] J. Bear, Y. Bachmat, *Introduction to Modeling of Transport Phenomena in Porous Media*, Kluwer Academic Publishers, Dordrecht, Boston, London, 1990.
- [36] V. Guinot, Multiple porosity shallow water models for macroscopic modelling of urban floods, *Advances in Water Resources* 37 (2012) 40–72. doi:10.1016/j.advwatres.2011.11.002.
- [37] B. F. Sanders, J. E. Schubert, H. A. Gallegos, Integral formulation of shallow-water equations with anisotropic porosity for ur-

- ban flood modeling, *Journal of Hydrology* 362 (1-2) (2008) 19–38. doi:10.1016/j.jhydrol.2008.08.009.
- [38] M. Bruwier, P. Archambeau, S. S. Erpicum, M. Pirotton, B. Dewals, A shallow-water model with depth-dependent porosity for urban flood modeling, in: *E-proceedings of the 36th IAHR World Congress*, The Hague, the Netherlands, 2015.
- [39] R. Hinkelmann, *Efficient Numerical Methods and Information-Processing Techniques in Environment Water*, Springer Verlag, Berlin, 2005.
- [40] B. R. Bird, W. E. Stewart, E. N. Lightfoot, *Transport Phenomena*, 2nd Edition, John Wiley & Sons, New York, USA, 2007.
- [41] H. M. Nepf, Drag, turbulence, and diffusion in flow through emergent vegetation, *Water Resources Research* 35 (2) (1999) 479–489. doi:10.1029/1998WR900069.
- [42] J. Hou, Q. Liang, F. Simons, R. Hinkelmann, A 2D well-balanced shallow flow model for unstructured grids with novel slope source term treatment, *Advances in Water Resources* 52 (2013) 107–131. doi:10.1016/j.advwatres.2012.08.003.
- [43] C. G. Mingham, D. M. Causon, High-resolution finite-volume method for shallow water flows, *Journal of Hydraulic Engineering* 124 (June) (1998) 605–614.

- [44] Q. Liang, F. Marche, Numerical resolution of well-balanced shallow water equations with complex source terms, *Advances in Water Resources* 32 (6) (2009) 873–884. doi:10.1016/j.advwatres.2009.02.010.
- [45] W. Zhang, T. W. Cundy, Modeling of two-dimensional overland flow, *Water Resources Research* 25 (9) (1989) 2019–2035. doi:10.1029/WR025i009p02019.
- [46] U. Razafison, S. Cordier, O. Delestre, F. Darboux, C. Lucas, F. James, A Shallow Water model for the numerical simulation of overland flow on surfaces with ridges and furrows, *European Journal of Mechanics - B/Fluids* 31 (2012) 44–52. doi:10.1016/j.euromechflu.2011.07.002.
- [47] S. Soares-Frazão, Y. Zech, Dam-break flow through an idealised city, *Journal of Hydraulic Research* 46 (5) (2008) 648–658. doi:10.3826/jhr.2008.3164.
- [48] J. E. Schubert, B. F. Sanders, M. J. Smith, N. G. Wright, Unstructured mesh generation and landcover-based resistance for hydrodynamic modeling of urban flooding, *Advances in Water Resources* 31 (12) (2008) 1603–1621. doi:10.1016/j.advwatres.2008.07.012.
- [49] B. Kim, B. F. Sanders, J. S. Famiglietti, V. Guinot, Urban flood modeling with porous shallow-water equations: A case study of model errors in the presence of anisotropic porosity, *Journal of Hydrology* 523 (2015) 680–692. doi:10.1016/j.jhydrol.2015.01.059.
- [50] V. Souchere, D. King, J. Daroussin, F. Papy, a. Capillon, Effects of tillage on runoff directions: consequences on runoff contributing area

within agricultural catchments, *Journal of Hydrology* 206 (3-4) (1998) 256–267. doi:10.1016/S0022-1694(98)00103-6.

- [51] O. Planchon, M. Esteves, N. Silvera, J.-M. Lapetite, Microrelief induced by tillage: measurement and modelling of Surface Storage Capacity, *Catena* 46 (2001) 141–157.